Pulsed Fission-Fusion (PuFF) – Phase I Report

Robert B. Adams, Ph.D.
National Aeronautics and Space Administration
George C. Marshall Space Flight Center

Jason Cassibry, Ph.D.
University of Alabama in Huntsville
Propulsion Research Center

David E. Bradley
Yetispace, Inc.

Leo Fabisinski
International Space Systems, Inc.

Geoffrey Statham, D.Phil.
ERC, Inc.

Executive Summary

In September 2013 the NASA Innovative Advanced Concept (NIAC) organization awarded a phase I contract to the PuFF team. Our phase 1 proposal discussed a pulsed fission-fusion propulsion system that injected gaseous deuterium (D) and tritium (T) as a mixture in a column, surrounded concentrically by gaseous uranium fluoride (UF6) and then an outer shell of liquid lithium. A high power current would flow down the liquid lithium and the resulting Lorentz force would compress the column by roughly a factor of 10. The compressed column would reach criticality and a combination of fission and fusion reactions would occur. The fission reactions would further energize the fusion center, and the fusion reactions would generate neutrons that promote more complete burnup of the fission fuel. The lithium liner provides some help as a neutron reflector but also acts as a propulsive medium, being converted to plasma which is then expanded against a magnetic nozzle for thrust. The expansion of the (primarily) lithium plasma against the nozzle's magnetic field inducts a current that is used to charge the system for the next pulse. Our concept also included secondary injection of a Field Reversed Configuration (FRC) plasmoid that would provide a secondary compression direction, axially against the column, and push the column away from the injection manifold, increasing the manifold's survivability.

Our phase 1 proposal included modeling the above process first under steady state assumptions and second under a time variant integration. We proposed including these results into a Mars concept vehicle and finally proposing promising conditions to be evaluated experimentally in Phase II. In phase I we quickly realized that we needed to modify our approach. Our steady state work was completed as proposed, and the results indicated that one, a two stage compression system was not needed and two, that we wanted to move away from UF6. The steady state model shows much more margin than expected, to the point that we may well reach breakeven with the Charger – 1 facility, a 572 kJ Marx bank currently under refurbishment at UAH. Additionally we found that using gaseous D-T and UF6, provided a relatively simple prospect of using a pulsed injector, made reaching criticality more difficult. The introduction of large amounts of fluorine meant a radiative sink, sapping power from the fusion plasma and was harder to handle. Therefore we moved to a solid uranium target that held D-T under pressure. In so doing we could move our target closer to criticality and remove any material that did not sustain the reaction.

However in moving to a solid target we complicated our time-variant model, now requiring us to develop phase change algorithms and stress-strain calculations for the solid matrix. We have continued efforts along this line but as expected we did not complete this model. After discussions with NIAC management we moved some of our resources to preparing existing equipment to support an experimental program testing various target configurations under a variety of z-pinches at different power levels. Contained in this report are our results preparing 200 J, 1kJ and 4-8 kJ pulsed power systems as well as a vacuum chamber and diagnostic equipment to evaluate generated plasmas.

We have also completed a point design of PuFF using the results of our steady state model. This design was then used to evaluate a couple missions of interest. At the behest of NIAC management we considered a more advanced version of the Mars mission, resulting in a vehicle that could reach Mars, one way, in 37 days with 25 mT of payload. This payload is consistent with a crew capsule or a Mars

lander. We envision PuFF being used to carry high speed payloads to an existing Martian base. We also considered a robotic probe to the outer solar system and interstellar space. This probe, using the same point design for the engine, carries 10 mT to 1000 AU in 36 years, enabling exploration of the local space around our solar system. These missions were the most obvious ones for the point design, and it should be stressed that there is significant potential to increase capability and performance. The PuFF team did not consider more optimization or additional missions, expecting that successful Phase II funding and execution will provide a more accurate relationship between target configuration, engine design and mission capabilities.

Finally we have put together our plan for future research, carried forward in a Phase II NIAC and beyond. As mentioned before concentrating on identifying the relationship between the target composition and geometry and the strength of the z-pinch is our highest priority. The composition and geometry will define the criticality of the target and potential energy release. The strength of the pinch defines the needed infrastructure to create the pinch, i.e. the engine mass. Both speak directly to the performance (specific impulse and specific power, respectively) of the concept. Our research plan, developed under Phase I, gives us the most economical path to determine these relationships and how to overcome limiting factors such as onset of plasma instabilities.

In conclusion our steady-state results to date have shown PuFF to be a powerful new propulsion system capable of meeting a range of different mission requirements. There is substantial research to be done to address the limiting factors inherent in the PuFF concept, which is reaching criticality and avoiding plasma instabilities. Our time variant model continues under development and we have put into place a number of physical apparatus to support a future test program of pinching targets at various power levels. The test program is laid out both here and our Phase II proposal and we continue development as resources permit to bring PuFF to fruition and enable the next phase of space exploration for the 21st century.

Contents

Introduction

The potential benefits of nuclear fusion propulsion have been well-documented for a range of exploration architectures covering missions to both the inner and outer solar system; however these benefits are often treated with skepticism because of concerns over the near-term practicality of controlled fusion. The present concept takes an emerging pure fusion concept being advanced by Sandia National Laboratories – the pulsed Z-Pinch – and uses the approach to compress a fission-fusion plasma to release nuclear energy at significantly less demanding conditions than are required for pure fusion.

The pulsed Z-Pinch is a device that is commonly used to compress laboratory plasma to high pressures (~1 Mbar) for very short timescales (~50 ns). An electrical discharge produces a high axial current along the outer surface of a column of plasma; this current in turn generates a very strong toroidal magnetic field. This 'self-generated' magnetic field interacts with the axial current – via the ($\underline{J} \times \underline{B}$) Lorentz force – and radially compresses the plasma column, bringing it to very high densities and temperatures.

Previously this team has explored a modified Z-pinch geometry as a propulsion system by encasing the plasma in a sheath of liquid lithium, providing a current return path. Results have been promising; the lithium acts as a temporary virtual cathode, and adds reactant mass for propulsion. Further, the lithium acts as a radiation shield against generated neutrons and gamma rays. Finally, we are able to tailor the density profile of the column using the lithium sheath. Recent theoretical and experimental developments (e.g. tailored density profile in the fuel injection, shear stabilization, and magnetic shear stabilization) have had great success in mitigating instabilities which would otherwise compromise the compression and fusion yield.

Despite the advantages offered by the Z-Pinch configuration, substantial power is still necessary to compress a deuterium-tritium (D-T) plasma to fusion break-even conditions. Calculations done under a 2010 Center Innovation Fund project indicate the minimum practical size for a Z-Pinch powered fusion propulsion system is of the order of 150 metric tons (mT). While this is an order of magnitude smaller than comparable fusion propulsion systems using laser inertial confinement or magnetic confinement, it is still only appropriate for use with crewed missions and deep space probes to near-interstellar space.

Our proposed concept uses the Z-pinch configuration explored above but uses a fission reaction to boost the fusion process. The column contains a central cylinder of D-T plasma, surrounded by a U-238 cylindrical sheath, which is in turn surrounded by a lithium cylindrical sheath. The D-T mixture is compressed until a limited number of fusion reactions take place (well below 'break-even' energy). The resulting fast thermonuclear neutrons bombard the surrounding U-238 and induce fission which in turn increases the fusion yield of the D-T core.

There is considerable synergy inherent in this concept. D-T are the easiest fusion fuels to ignite, but are the least desirable because most of the energy release is in the form of high-speed neutrons, which are of little use for power generation or thrust and damage the propulsive structure. In the proposed concept the neutrons from both fission and fusion reactions are well reflected and moderated by the lithium liner. Also the neutron release from fusion will result in more complete consumption of the fissile fuel, sustaining energy release. The sustained release extends the compression of the fusion reactants, yielding more fusion reactions. And of course more fusion release means more neutrons for

more fissile consumption. This fortuitous cycle means that the fission event is not simply used to ignite fusion, but also helps achieve a more complete burn-up of the fission and fusion fuels. This synergy has been observed in the development of other fission-fusion devices.

Using fission-fusion synergy means that ignition may be achieved with lower energy input through the Z-pinch. Lower energy input will translate into smaller capacitor banks and a smaller overall propulsion system. The proposal team hopes to develop a considerably smaller hybrid propulsion system. A smaller system would be considerably less expensive to develop and would be applicable to a wider range of NASA missions. Also, while the concept of the fission-fusion hybrid is rooted in weapons design, our concept has built in non-proliferation features. Even with the reductions in size our team hopes to achieve with this concept, it will still be far too large to ever be a terrorist weapon. Finally the propulsion system has a built in method to vary specific impulse. Trading specific impulse for thrust is desirable when optimizing a trajectory. By varying the thickness of the lithium liner our concept can easily increase thrust (at the expense of specific impulse).

Background

The idea of combining fission and fusion, so that the former process assists the latter, is well established – most obviously in the field of nuclear weapons; however, it has seen relatively little application in the field of space propulsion. The most obvious exception was Project Orion, during the late 1950s and early 1960s, which proposed to expel thermonuclear bombs from the base of a very large vehicle and detonate them a short distance away. The resulting blast wave would then impact a 'pusher' plate at the rear of the vehicle, and thrust would be transmitted to the vehicle by means of a set of shock absorbers.

Project Orion has been well-documented – see, for example, Ref. 1 – and was intended to use actual thermonuclear weapons, rather than a wholly unique design, so it will not be considered further here; however, there are several more recent concepts – *not* utilizing weapons hardware – which are of more relevance to PuFF. Before reviewing them it is instructive to establish a simple taxonomy of fission-fusion hybrid systems as follows.
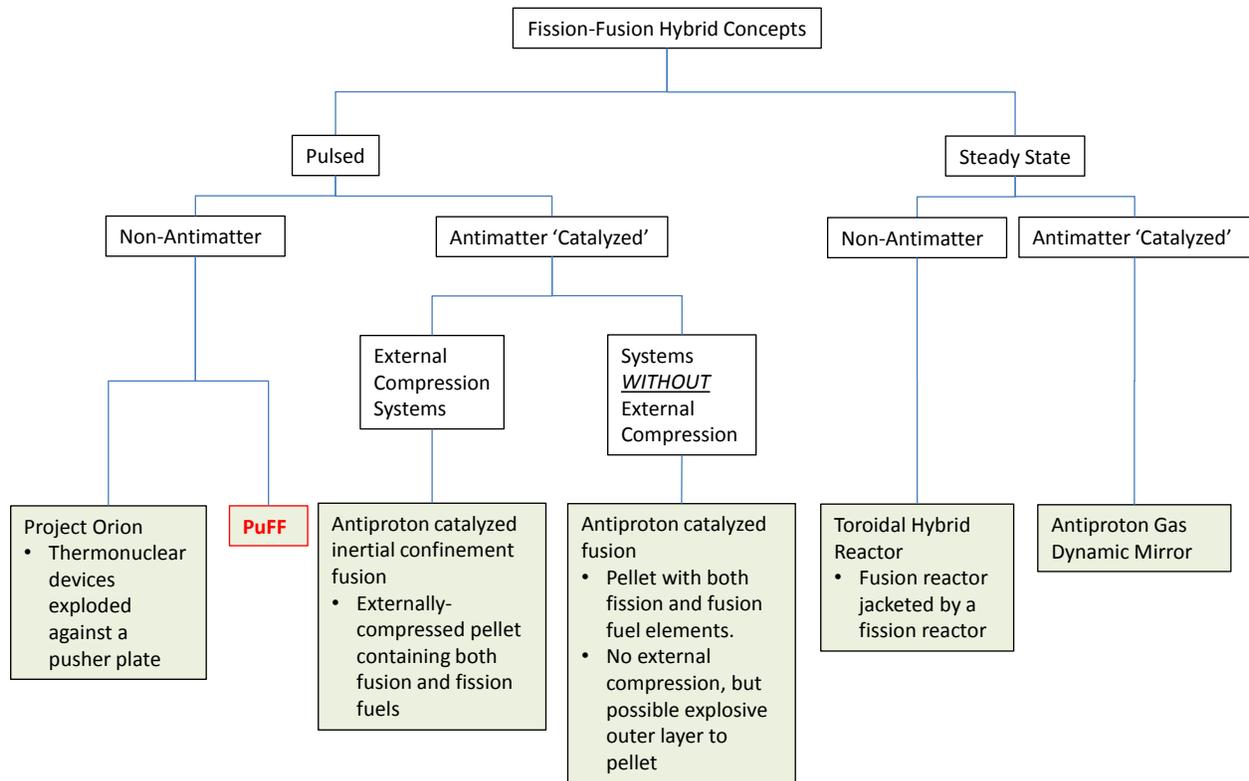

Figure 1 – Taxonomy of Fission-Fusion Hybrid Propulsion Concepts

There are two major groups by which the concepts can be categorized: whether they operate in pulse mode or steady state, and whether or not they make use of antimatter.

Taking the pulse-mode operation group first, the two *non*-antimatter concepts are Orion, which was described earlier, and PuFF. The antimatter-based concepts all make use of the fact that both uranium and plutonium nuclei can be made to fission by an antiproton. This occurs because the antiproton annihilates with one of the nucleons (either a proton or a neutron) and the resulting energy release will

break up the remainder of the nucleus. This will take place regardless of the size of the uranium or plutonium sample – there are no critical mass considerations – and the fission will also release a number of neutrons, which can cause subsequent fissions in the surrounding nuclei.

Although there are now a number of papers proposing antimatter-catalyzed pulse-operated concepts, they appear to fall into two basic categories: those that require an external compression system – of the type used in inertial-confinement fusion – and those in which the pellet is self-contained.

The principal inertial-confinement concept, Antiproton Catalyzed Inertial Confinement Fusion (see Ref. 2), makes use of an 8 mm diameter target pellet which is filled with 77 mg of an equimolar mixture of deuterium and tritium, together with 680 mg of plutonium. The pellet has a gold shell.

Core:
• 4000 µm radius
• Contains:
    • 77 mg of DT (equimolar mixture)
    • 680 mg of plutonium
Shell:
• 80 µm thickness
• Consists of gold
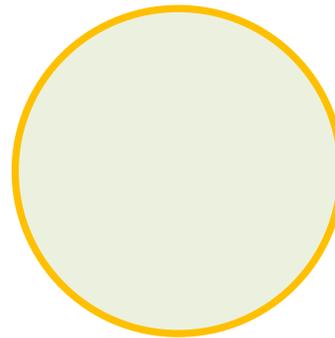
Figure 2 – Target Pellet for Antiproton Catalyzed Inertial Confinement Fusion

The target is compressed by converging beams of lithium ions, which ablatively heat the outer portion of the shell. The inner portion of the shell acts as a radiation barrier to prevent bremsstrahlung radiation (from the ablatively-produced plasma) from pre-heating the core of the target.

The lithium ion beams produce a pressure of 11,000 Mbar. The resulting density and radius of the target are 1000 gm/cc and 510 µm; the confinement time of the target is 12 nsec.

After the core of the target has been compressed, a burst of 10^7 antiprotons is fired into it. This should produce 10^7 fission events and 10^8 neutrons – which induce additional fissions.

Fissions dominate initial energy release – up until about 11.9 nsec. At this time the core temperature reaches 2 keV and the fusion rate becomes comparable to the fission one. Note that the 14 MeV fusion neutrons will initiate additional fissions. The last 99.7% of both the DT and the plutonium will be consumed in the final 100 psec.

The output energy is about 76 GJ (compared with the 1.1 MJ of input energy, this gives a gain of 69,000). Half of this energy comes from fissions and half from fusions.

Ref. 2 proposed a vehicle carrying 100 Penning Traps, to store the antiprotons. Each trap would contain 10^{10} antiprotons. The propulsion system would pulse at a rate of 0.1 Hz, and would use 10^7 antiprotons per pulse.

The principal concept that does not require external compression was introduced in Ref. 3 and then refined in several subsequent papers. In this case the pellet design is as shown below.


Fusion Fuel: D-T or lithium deuteride

Outer layer: dense, high-temp. material (e.g. tungsten)

Inner layer: neutron-generating or reflecting material (e.g. uranium)

R_F

$2a$

δ

R_C

Electrically-neutral beam of antiprotons and positrons

Fissionable material (^{235}U, ^{238}U or ^{239}Pu)
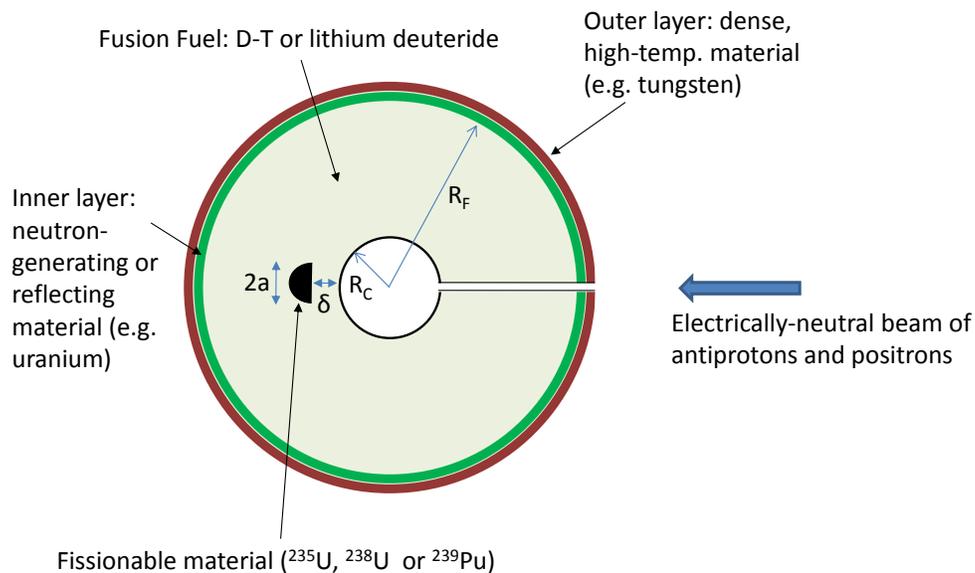
Figure 3 – Advanced Target Pellet for Antiproton Catalyzed Inertial Confinement Fusion

The shell consists of an outer layer, which is made of a very dense, high-temperature material, such as tungsten. Within this is a layer of a neutron-reflecting or neutron-generating material such as uranium. The bulk of the pellet is filled with a fusion fuel, either a deuterium-tritium mixture, or lithium deuteride, and there is a cavity at the very center, with a single hole extending out to the surface. In line with the hole is a small chip of fissionable material.

As shown in Figure 3, a beam of antiprotons and positrons is directed into the hole. The positrons do not play any significant part in what follows, and they are included so as to simplify the beam dynamics by ensuring electrical neutrality. The antiprotons annihilate at the flat surface of the small chip of fissionable material. The annihilations will cause the heavy nucleus to undergo fission; with a consequent release of fission fragments, neutrons and energy. The energy release ionizes the portion of the fusion fuel between the core and the fissile hemisphere.

In addition, the annihilation will produce neutral and both positively- and negatively-charged pions. The neutral pions will decay rapidly into gamma rays, while the charged pions will decay into charged muons and neutrinos.

As shown below in Figure 4, the core of the pellet fills with the plasma created as a result of the annihilation.
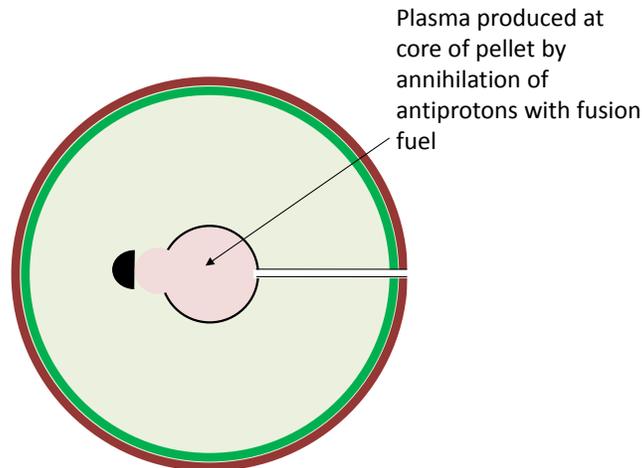
Figure 4 – Plasma Generation at Target Core

Both ions and electrons in this plasma will move away from the annihilation site, but the electrons will move more quickly, thus producing a short, but very intense net electrical current. The current will generate a very intense transient magnetic field in the core region of the pellet. The magnetic field traps the various charged particles (fission fragments, electrons, light ions, pions and muons) in this region and thus allows the plasma to come up to fusion temperatures, with the tungsten shell containing the contents long enough for the fusion reaction to go to completion. A shock wave propagates outwards through the pellet. The fusion reaction proceeds for approximately the same time as it takes the shock to propagate through the pellet.

Note that the neutrons produced during fission (on the flat face of the hemisphere) can go on to induce additional fissions in the rest of the hemisphere as well as the uranium shell. Also note that the uranium shell will reflect some of the neutrons back into the center of the pellet. It will also generate neutrons itself, which will go into the central regions.

A modified version of this concept is presented in Ref. 4. The pellet is redesigned, as shown below in Figure 5, to incorporate a layer of explosive between the outermost (tungsten) shell and the inner shell of uranium or plutonium. In addition the fusion fuel is now definitely selected as being lithium deuteride.

Fusion Fuel: Lithium Deuteride

Outer layer: dense, high-temp. material (e.g. uranium or tungsten)

Inner layer: uranium or plutonium

Electrically-neutral beam of antiprotons and positrons

Explosive layer (TNT)

Fissionable material (^{235}U, ^{238}U or ^{239}Pu)
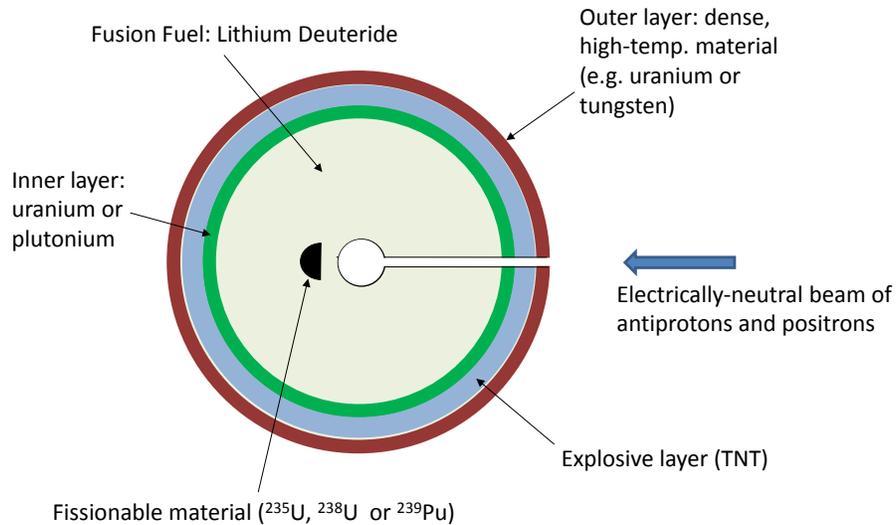
Figure 5 – Redesigned Pellet with Explosive Jacket

There are two main consequences of the pellet design modification. The first is that, after fusion has commenced, the pulse of neutrons that moves outwards can induce additional fission reactions in the inner shell of uranium or plutonium. These reactions, which can continue until the mechanical shockwave (from the central region) reaches the shell, will improve the total energy release from the pellet.

The second design modification, the explosive shell, will improve the fusion rates by increasing fusion fuel density after it has detonated. It will also serve to slightly increase the overall confinement time.

The steady-state fission-fusion concept that has received most attention is not associated with space propulsion, but instead with the more complete burning of nuclear fuel and consequent alleviation of current waste disposal problems (see Ref. 5). It consists of a fusion reactor that is jacketed with a fission reactor. A possible configuration is shown in simplified form below in Figure 6 (note that the power-extraction parts of the design are omitted for clarity).
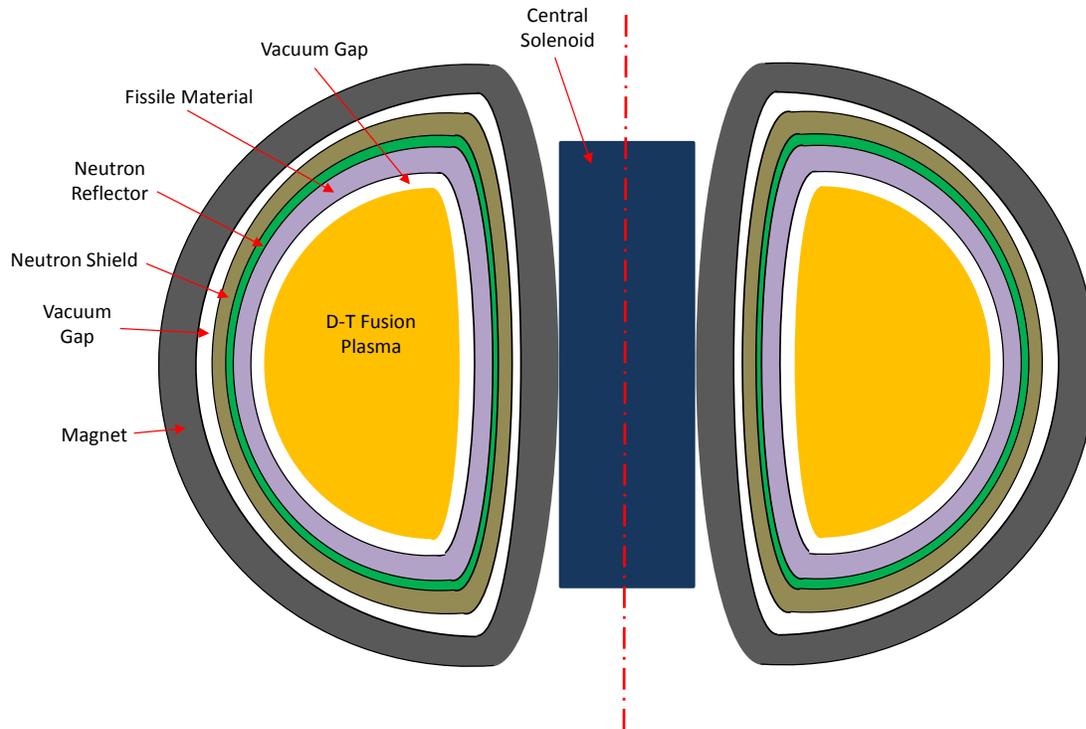
Figure 6 – Fission-Fusion Hybrid Tokamak Reactor Concept

The concept involves bringing a deuterium-tritium (D-T) plasma up to fusion conditions in a toroidal confinement chamber. Unlike a pure fusion reactor, which would need to achieve a large energy gain (output power divided by input power) to be viable, the D-T reactions in a hybrid device are primarily required to produce neutrons – something that they do very readily.

The 14.1 MeV neutrons that are liberated during D-T fusion will bombard the fission reactor that jackets the fusion chamber and lead to a much more complete 'burn-up' of the fission fuel (uranium or plutonium). In a conventional fission reactor the fuel rods degrade as the atoms break up into fission fragment by-products. The rods become unusable when they still contain a large quantity of fissile fuel and need to be removed. Although the remaining fissile fuel can be recovered, the recycling process is very expensive.

In a hybrid reactor the fusion-produced neutrons will continue to fission the remaining fissile atoms even when most of the fuel rod has been used up. Not only will this extend the life of the rods, and enable a much more complete use of the fissile fuel, but it will simplify the eventual disposal of the spent rod – as a much greater proportion of the fuel will have been utilized.

A modified version of this concept might involve replacing the jacket of fissile material with thorium. Under neutron bombardment this would transmute into ^{233}U, which could then itself be made to fission by a subsequent neutron impact.

The final steady state concept shown in the organizational (taxonomy) diagram (Figure 1) – the Antiproton Gas Dynamic Mirror – refers to a number of similar concepts (see Refs. 6, 7 and 8). All of

these concepts consist of a Penning Trap, connected to a Gas Dynamic Mirror (GDM), which is in turn connected to a magnetic nozzle (as shown below in Figure 7).

U-238

Penning Trap
(contains
antiprotons)

Gas Dynamic
Mirror

Small flow of
antiprotons out of
trap and into mirror

Antimatter induced
fission of uranium

Magnetic Nozzle
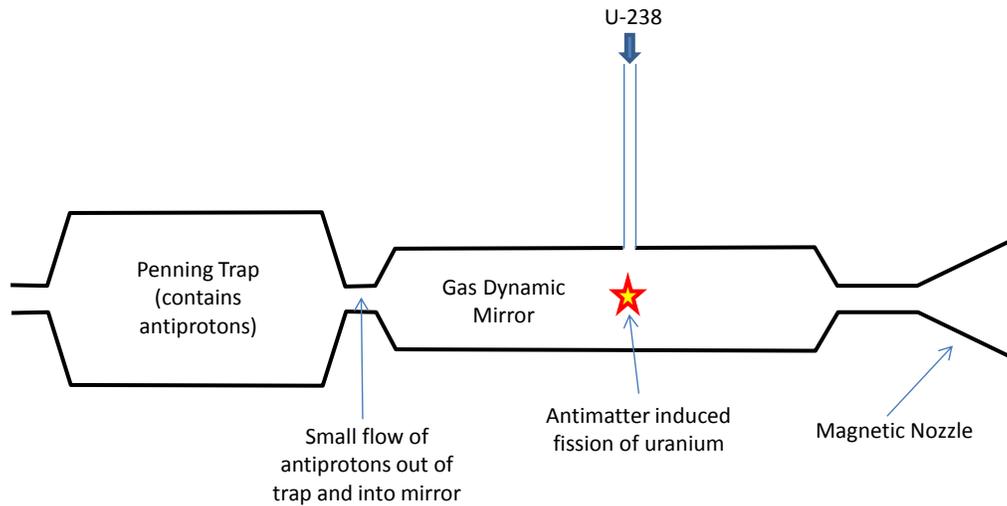
Figure 7 – Antimatter-Induced Fission Concept

In the simplest variant of this concept, antiprotons leak out of the Penning trap and enter the GDM, where the magnetic field constrains them to travel along the main axis until they intercept a stream of U-238 atoms, which is injected as shown above. The antiprotons will annihilate with some of the uranium nuclei and will cause them to fission. Neutrons produced by these primary fissions will then cause additional fissions to take place in the surrounding atoms. The fission products (i.e. fission fragments) will then serve to ionize and heat up the remaining uranium atoms (that do not undergo fission) and the entire plasma – with all its components – will be accelerated out through the magnetic nozzle.

In this most basic form the concept does *not* involve any fusion reactions, but in a modified version (see Figure 8 below) the GDM would also contain a deuterium-tritium plasma.
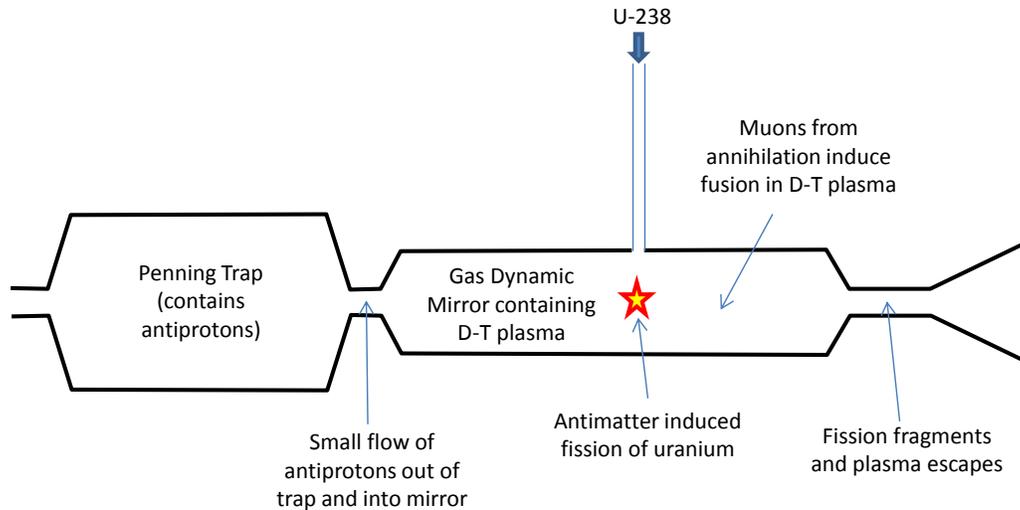
Figure 8 – Antimatter-Induced Fission-Fusion Concept

Among the products of the antiproton-induced uranium fission are positively and negatively charged pions. These decay very rapidly into muons, which are also charged and which are then capable of inducing fusion within the D-T plasma. The mechanism by which this takes place is that a negatively charged muon – having the same electrical charge as an electron – can replace the electron in a deuterium or a tritium atom. Although electrically identical to the electron, the muon has a much greater mass (approximately 200 times greater). This increased mass brings the muon into a much lower orbit around the nucleus, which effectively reduces the electrostatic repulsion between two adjacent atoms. This permits the two nuclei to come much closer to each other, and effectively reduces the repulsion barrier that normally makes fusion so difficult to achieve. In this form, the concept is referred to as 'muon-boosted fusion propulsion' – although the uranium fission is a necessary part of the overall process, so it does qualify as a hybrid fission-fusion concept.

[Note that there may be a significant barrier to this process because there is a high chance that a muon will bind with an alpha particle – produced by an earlier fusion event – rather than with a deuterium or tritium nucleus.]

One additional modification has been proposed, in which the GDM is jacketed with thorium, as shown below in Figure 9.

U-238

Neutrons from fusion in D-T plasma bombard thorium jacket and breed uranium, which can subsequently fission

Thorium jacket

Penning Trap (contains antiprotons)

Gas Dynamic Mirror containing D-T plasma

Antimatter induced fission of uranium

Small flow of antiprotons out of trap and into mirror

Fission fragments and plasma escapes

Muons from annihilation induce fusion in D-T plasma

Figure 9 – Antimatter-Induced Fission-Fusion Concept with Thorium Jacket

In this variant the high energy neutrons liberated during deuterium-tritium fusion – instead of passing out of the system – is allowed to bombard the jacket and cause some of the thorium atoms to transmute into uranium-233. The U-233 atoms can then be fissioned by the impact of another neutron, thus releasing energy. This technique – which is technically an antimatter-fission-fusion-fission concept – has been proposed both as a means of improving propulsion performance (by using the fission thermal energy to heat hydrogen) and as a means of providing an electrical power source for use during operations at the vehicle destination.

Set against the above concepts, PuFF manages to create a mutually beneficial interaction between fission and fusion, but with rather less complexity and technical 'overhead':

- It does *not* require a target pellet that needs to be engineered with high precision;
- It does *not* require antimatter;
- It does *not* require a toroidal confinement chamber, with the associated electromagnets.

Results

Our phase 1 proposal included modeling the above process first under steady state assumptions and second under a time variant integration. We proposed including these results into a Mars concept vehicle and finally proposing promising conditions to be evaluated experimentally in Phase II. Each of these sections (steady state model, time variant model, concept vehicles and experimental design) are discussed in further detail below.

Integrated Steady State Model (Lindl-Wagner Diagram)

In the theoretical analysis, we are modeling fission and fusion energy released in so-called 'targets'. These consist of a magnetized plasma surrounded by layers of lithium and either uranium or thorium. To assess feasibility we need to determine the density, temperature, and thickness of each of these layers in order to find the regions of parameter space in which the system leads to a net heating of the target. The power balance is

$$\frac{dE}{dt} = P\frac{dV}{dt} + f_\alpha Q n^2 \langle \sigma \upsilon \rangle V - P_{brems} - P_{sync} - Ak\nabla T$$

where P is the pressure, V is the target volume, f_α is the fractional deposition of alpha particles, Q is the fusion reaction energy, n is the particle number density, $\langle \sigma \upsilon \rangle$ is the velocity averaged cross section for the fusion reaction, A is the target surface area, k is the thermal conductivity, and T is the temperature. P_{brems} represents Bremsstrahlung radiation loss given by

$$P_{brems} = 1.44e^{-40}n^2 T^{\frac{1}{2}} V$$

and P_{sync} represents synchrotron radiation loss given by,

$$P_{sync} = 5.342e^{-24}nB^2 T(1 + \frac{T}{2.367e^9})V$$

The first term (PdV/dt) represents the work done by the compression of the liner on the target. The second term is the power from fusion reactions. The last term is the thermal conduction loss.

Briefly, we assume a cylinder of plasma with a DD or DT mixture, and vary the temperature and density. We investigated the effects of [235]U, [238]U, [232]Th, and [6]Li liners on DT gas targets with a magnetic field comparable to what would be generated by a 2 MA Z-pinch produced in the Charger 1 facility. For the DT plasma, we assumed all neutrons pass through the surrounding liner with an energy of 14.1 MeV. The high Z materials all yield reactions with ~160 MeV of fission fragments per reaction, while the lithium produces 4.784 MeV per reaction. The neutron fission cross sections were taken from the Evaluated Nuclear Data File (Ref. 9).

(a)   (b)
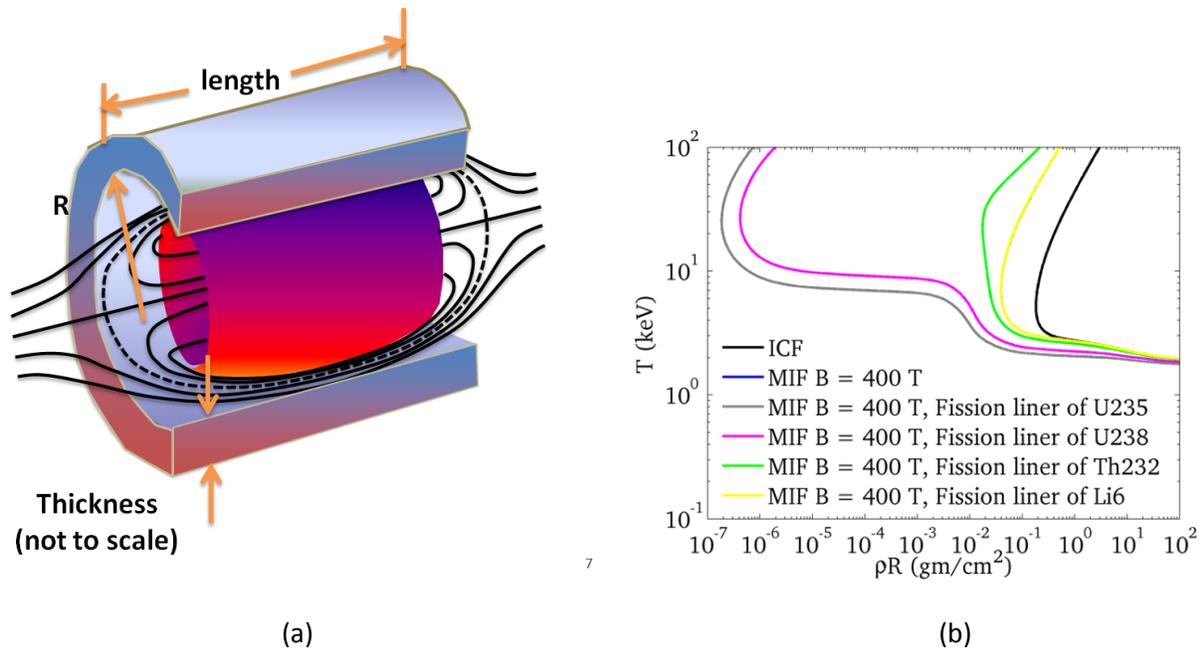
Figure 10. (a) Sketch of fission/fusion hybrid target. Magnetic field embedded in fusion target (center object), surrounded by a fissionable liner of Uranium, Thorium, or ^{6}Li. (b) Contours for net power (fast fission + fusion) balancing against radiation and thermal conduction losses in ρR vs T space, where ρ is fusion target mass, R is the fusion target radius, and temperature is the fusion target temperature.

The contour in Figure 10 shows the region in which the net power produced by nuclear reactions exceeds the loss mechanisms in ρR vs T space. The black contour line is labeled 'ICF' and represents the typical region for net power production for inertial fusion. Generally, there is no embedded magnetic field. Beneath the contour (3 to 5 keV) the fusion power is not significant and the radiation and thermal conduction readily cool the target. The 'nose' on the left of the contour is primarily controlled by electron thermal conduction, which overtakes the fusion power at low densities. Above the contour, high temperatures lead to enhanced radiative cooling. When the target contains a magnetic field, the cross-field thermal conduction is suppressed, lowering the required ρR and shifting the contour to the left. This result is highly dependent on the magnitude of the magnetic field. The effects of fission power are very apparent in this figure. For the cases investigated, we found that a target with radius 1 mm and surrounded by a 5 mm liner gave very promising results for both uranium isotopes. Specifically, the region of positive power production extended beyond the range of densities investigated. This is due to the relatively high fast fission cross sections for both of these isotopes, and the power is dominated by the fission power initiated by fast neutrons produced in the DT fusion reactions. The reason that the fission power is greater is that the energy per reaction is about 20 to 100 times greater (160 MeV compared to a few MeV) per reaction.

To illustrate how this power balance can be used, we select a region of the ρR space where there is net heating for the hybrid target, 1×10^{-4} gm/cm^2 and T = 15 keV. By selecting a fusion target radius and length, this sets the density, mass, and internal energy of the fusion target. We can then vary the target

radius and plot versus the total thermal energy and fusion target mass required. As Figure 11 shows, the initial thermal energy is linear with radius as shown, while the initial target density decreases. There are two takeaways from this exercise. First, the target energy for fusion is reduced to potentially 1 kJ or less, and the target density varies from liquid down to roughly the density of air. These parameters are well within reach, and such states can readily be tested with existing hardware at MSFC and UAH.
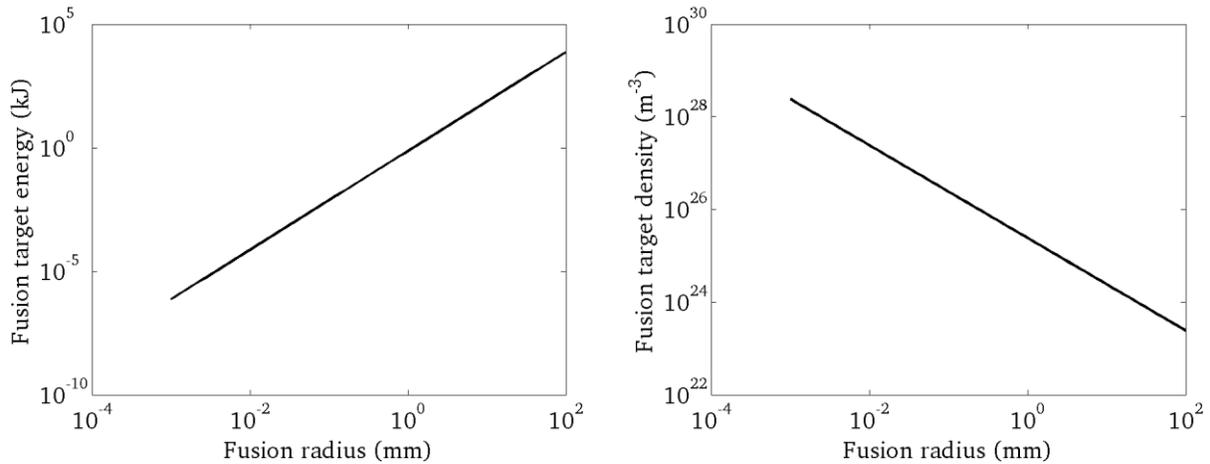
Figure 11. Scaling of DT fusion target energy (left) and number density (right) with radius for $\rho R = 1 \times 10^{-4}$ gm/cm^2, T = 15 keV, and an assumed DT/Uranium hybrid target.

From these charts we can develop a point design of the target. Typical pinch lengths in the literature are ~2 cm, so we select that for the target length. Assuming a 10 to 1 compression ratio of the DT target, we have selected peak stagnation conditions needed and worked backwards. At full compression, the DT needs to be at 1000 kg/m^3, which is the same as liquid water. Such densities have a relatively short topping distance for the fusion charged particles, so local deposition of some of the energy will occur, helping to maintain fusion temperatures. Uncompressed, the initial target radius for DT will then be 1 mm, with cold density of 10 kg/m^3. This needs to be surrounded by a liner of ^{238}U. At solid density, we have determined (using the power balance diagram above), that the thickness needs to be at least 4 mm under the conservative assumption we have made that neutrons from DT fusion reactions only make a single pass, and that no chain reaction or secondary reactions boost the liner. An important element of the phase II study will be to determine under what circumstances, if any, would a chain reaction take place that may further reduce the required input power. If the pinch directly drives the uranium liner, we have found that a 3 to 1 shock compression of the uranium in a cylindrical geometry would require an initial thickness of only 3mm per target, compressed to a thickness of 1 mm. Whether or not we can achieve such a compression while transferring sufficient energy to the DT target with our existing hardware is not yet known, and the Phase II study will help us to answer these questions. It should be emphasized that such compression isn't critical to demonstration of proof of principle, but will help lower the total energy and power requirements if feasible. Our proposed hybrid target is a 0.63 µg 1 mm thick DT target surrounded by a 3 mm thick 11.46 gram depleted uranium liner. To augment the fast neutron fission reactions, we may include a coating of 6Li in between these layers, or surround the target with 7Li coating. The former will breed tritium to help boost the fusion reactions, while the latter

will breed additional neutrons to burn the outer layers of the uranium liner via reactions with the interior 14.1 MeV neutrons that do not get scattered in the uranium liner.

Integrated Time Variant Model

SPFMax Development

A smooth particle hydrodynamic code was completed and utilized for the Phase I effort. We leveraged development on another contract, but performed a significant amount of verification related to the present effort. SPH is a Lagrangian fluid code in which Euler, or Navier Stokes equations are solved on a discrete set of point masses which move at the local bulk velocity of the fluid. The primary advantage of the approach is the ability to accurately resolve fixed masses with distinct boundaries between gas and vacuum, and obviates the need for a computationally expensive grid for the space surrounding the system to be studied. Further, the SPH approach is naturally adaptive, and as a result, we have found that large, complex 3D problems can be modeled with just a few thousand particles and yet achieve accuracies within 10% of exact solutions for test cases.

The code we are developing is called Smoothed Particle Fluid with Maxwell equation solver (SPFMax). SPFMax is a hybrid between a smooth particle hydrodynamic plasma fluid solver and a 3D time dependent Maxwell equation solver utilizing the finite difference time domain method.

The partial differential equations are discretized using the smoothed particle formulation, which will be discussed below. We have developed the equations of motion and implementation strategy for the physics/chemistry model of electrically-controlled solid propellants (ESP). The flow solver is based on the following equations describing the motion of gases and ionized particles which will be present in the ESP experiments,

$$\left(\frac{\partial}{\partial t} + \mathbf{u_e} \cdot \nabla \right) n_e + \nabla \cdot \mathbf{u_e} = 0 \tag{1}$$

$$\left(\frac{\partial}{\partial t} + \mathbf{u_i} \cdot \nabla \right) n_i + \nabla \cdot \mathbf{u_i} = 0 \tag{2}$$

$$n_e m_e \left(\frac{\partial}{\partial t} + \mathbf{u_e} \cdot \nabla \right) \mathbf{u_e} + \nabla p_e + e n_e \left(\mathbf{E} + \mathbf{u_e} \times \mathbf{B} \right) = -\nabla \pi_e + \mathbf{R_e} \tag{3}$$

$$n_i m_i \left(\frac{\partial}{\partial t} + \mathbf{u_i} \cdot \nabla \right) \mathbf{u_i} + \nabla p_i - Z e n_i \left(\mathbf{E} + \mathbf{u_i} \times \mathbf{B} \right) = -\nabla \pi_i - \mathbf{R_e} \tag{4}$$

$$\frac{3}{2} n_e \left(\frac{\partial}{\partial t} + \mathbf{u_e} \cdot \nabla \right) k T_e + p_e \nabla \cdot \mathbf{u_e} = -\pi_e : \nabla \mathbf{u_e} - \nabla \mathbf{h_e} - \left(\mathbf{u_e} - \mathbf{u_i} \right) \cdot \mathbf{R_e} - Q_i \tag{5}$$

$$\frac{3}{2}n_i\left(\frac{\partial}{\partial t}+\mathbf{u_i}\cdot\nabla\right)kT_i+p_i\nabla\cdot\mathbf{u_i}=-\pi_i:\nabla\mathbf{u_i}-\nabla\mathbf{h_i}-Q_i \qquad (6)$$

where the subscripts e and i refer to electrons and ions, respectively, **u** is the velocity, n is the number density, m is the electron or ion mass, p is the pressure, **E** is the electric field, **B** is the magnetic field, Z is the ion charge, k is the Boltzmann's constant and T is the temperature. The dissipative terms consist of the friction for $\mathbf{R}_e$, viscous stress tensor π, thermal conduction **h**, and the thermal equilibration term Q_i. Also note that the resistive dissipation term is $\left(\mathbf{u_e}-\mathbf{u_i}\cdot\right)\mathbf{R_e}$. Expressions for the dissipation terms can be found, for example, in (Hans Goedbloed and Stefan Poedts 2004). Similar equations can be developed for neutrals.

One of the most significant technical challenges to such a model is accounting for electromagnetic field effects in propellant motion and chemistry. Most fluid codes using computational fluid dynamics (CFD) or magnetohydrodynamcs (MHD) are unable to include the required physics. Particle-in-cell (PIC) codes are potentially able to model ESP, however, they are unable to conduct parametric studies because each simulation requires prohibitively large computational resources. This hybrid electromagnetic/smooth particle hydrodynamic code approach simultaneously permits modeling all the required physics while being able to run 3D simulations in a few hours on a workstation.

Several methods can be employed to solve complex engineering problems. Numerical modeling techniques are useful when solving multidimensional partial differential equations that are too difficult to solve by hand. When it comes to fluids, numerical modeling generally explains behavior using Eulerian, Lagrangian, or combination models by means of fixed-point grids. However, grid-based simulations are not efficient or practical when solving problems involving highly deformable substances (Ala and Francomano, 2011). Problems are exacerbated when complex geometries and free spaces interact with deformable surfaces of fluids. Remeshing and additional mathematical processes may be required to produce an accurate model. These additions are extremely computationally taxing and time-consuming. When multiple fluids and processes are interacting with one another, meshes can no longer be used to illustrate the effects of the interactions. It becomes necessary to utilize mesh-less methods that account for conservation laws while accurately illustrating physical processes.

Mesh-less numerical models use a domain of arbitrarily placed nodes or particles to approximate solutions to partial differential equations (Ala and Francomano, 2011). Each particle carries the physical properties of a fluid or solid being tested. Particle interaction is observed over time in a purely Lagrangian sense which illustrates a more complete picture of overall behavior. Smoothed particle hydrodynamics (SPH) is a mathematical modeling technique that employs mesh-less strategies to solve complex differential equations. SPH approximates functions of physical properties by interpolating a continuous kernel over a domain of particle locations. The formula for the function approximation is

$$A_a(\mathbf{r})=\int A(\mathbf{r}')W((\mathbf{r}-\mathbf{r}'),h)\,d\mathbf{r}' \qquad (7)$$

where W is the kernel, h is the smoothing length or the distance of influence from particle a, and **r** is the position of the particle. The integral function can be numerically summed over a compact support domain of particles.

$$A_a(r) = \sum_b m_b \frac{A_b}{\rho_b} W(r - r_b, h) \tag{8}$$

For example, to calculate certain properties for particle b, the property being solved for, A, is divided by the density, ρ, and multiplied by the mass, m, and the kernel function. Accurate approximation depends primarily on the smoothing length, h. If the smoothing length is too small, interpolation of nearby particles would not be possible, or rather the simulation would not be able to detect the effects that nearby particles would normally have on one another. If the smoothing length is too large, then certain groups of particles would be seen affecting one another that normally would not (Ala and Francomano, 2011). Error must be minimized by discretizing the space around particles through differentiation of the property function.

$$\nabla A_a(r) = \sum_b m_b \frac{A_b}{\rho_b} \nabla W(r - r_b, h) \tag{9}$$

While grids inherently provide discretization for finite element models, the SPH kernel enables the space around particles to be discretized without the need for meshes, making SPH extremely versatile (Ala and Francomano, 2011). Further refinement of discretized space is possible through higher order differentiation which also reduces error at the cost of computation time. So to reiterate, property approximation depends completely on the smoothing kernel which, in turn, is a function of the smoothing length.

SPH was first developed in 1977 by Lucy, Monaghan, and Gingold as a method to reproduce equations of motion with more natural particles by means of kernel estimation techniques already in practice (Monaghan, 2005). Later development allowed SPH to automatically account for conservation laws, providing a path for utilization in most scenarios involving fluid dynamics, whereas, before, SPH could only be used to solve certain types of astrophysical problems (Monaghan, 2005). Today, SPH models are used extensively in a variety of fluids, elasticity, and fracture problems (Monaghan, 2005). It has even become a staple in the special effects industry for film and video games (Monaghan, 2005). Because of its versatility and accuracy, new adaptations of SPH are being created and tested every year to solve advanced problems in scientific arenas that have never experienced SPH treatment previously.

In engineering, multiple fluid interactions are extremely common, especially when chemical reactions are catalysts to electromechanical work. Propulsion sciences, especially, experience multiple fluid interactions on a regular basis. While simple numerical models help to show proof of concept, detailed chemistry and fluid models of combustion reactions have been difficult to produce with conventional methods. Furthermore, concurrently interacting physical processes have never been modeled in detail using consistent numerical methods. However, using SPH methodologies, it is possible to show particle interaction in the physical sense, not only between multiple fluids, but also between circuit-chemistry

reactions. SPFMax is a program that uses SPH algorithms to simulate interacting fluids. New modifications to SPFMax have been able to produce smoothed particle electromagnetics (SPEM) models of circuits that illustrate current propagation through electrode solids. The circuit model is designed to interact with charged particles in a fluid – a truly novel concept. With SPFMax, several types of electric propulsion could potentially be modeled on a particle level. Additionally, with the added detail of the mesh-less Lagrangian methods employed by SPFMax, propulsion systems entering the conceptual stage could be modeled in detail and modified for maximum efficiency before small scale models are even built. The ultimate goal in development of SPFMax is to make novel and highly conceptual propulsion designs more accessible and cheaper to develop into fully integrated systems.

Early on in development of SPH, several non-hydrodynamic applications were explored, including modeling Maxwell's curl equations. This eventually led to the development of smoothed particle electromagnetics (SPEM). Like SPH, SPEM was created to solve complex problems without the need for meshes. In this manner, SPEM is a direct alternative to circuit modeling techniques like finite difference time domain methods. SPEM models solve Maxwell's equations over a domain of randomly spaced particles, just as SPH models are used to solve fluid dynamical equations. Maxwell's electric and magnetic field equations are

$$
\nabla \times \mathbf{H} = \frac{\partial \mathbf{E}}{\partial \mathbf{t}} + \mathbf{J}
$$
$$
\nabla \times \mathbf{E} = -\mu \frac{\partial \mathbf{H}}{\partial \mathbf{t}}
$$
(10)

where **H** represents the magnetic field, **E** – the electric field, **J** – the current density, and μ is the permeability of circuit material. Calculating changes in electric and magnetic fields is rather different from calculating physical properties such as temperature and density in that changes depend on field strengths of the neighboring particles. In other words, electric field changes depend on the strength of the magnetic field in neighboring particles, whereas magnetic field changes depend on the strength of the electric field in neighboring particles. This observation is more readily apparent in the expanded curl equations in the *x*, *y*, and *z* directions, where new variables ε, σ, and *V* represent the permittivity, conductivity, and volume of the circuit material respectively.

$$
\frac{\partial E_x}{\partial t} = \frac{1}{\varepsilon} \sum_{j=1}^{N} \left(H_z\left(r_j^H\right) W_y^E - H_y\left(r_j^H\right) W_z^E \right) V_j + \frac{\sigma E_x\left(r_i^E\right)}{\varepsilon} - \frac{J_x}{\varepsilon}
$$

$$
\frac{\partial E_y}{\partial t} = \frac{1}{\varepsilon} \sum_{j=1}^{N} \left(H_x\left(r_j^H\right) W_z^E - H_z\left(r_j^H\right) W_x^E \right) V_j + \frac{\sigma E_y\left(r_i^E\right)}{\varepsilon} - \frac{J_y}{\varepsilon}
$$
(11)

$$
\frac{\partial E_z}{\partial t} = \frac{1}{\varepsilon} \sum_{j=1}^{N} \left(H_y\left(r_j^H\right) W_x^E - H_x\left(r_j^H\right) W_y^E \right) V_j + \frac{\sigma E_z\left(r_i^E\right)}{\varepsilon} - \frac{J_z}{\varepsilon}
$$

$$\frac{\partial H_x}{\partial t} = \frac{-1}{\mu} \sum_{j=1}^{N} \left(E_z\left(r_j^E\right) W_y^H - E_y\left(r_j^E\right) W_z^H \right) V_j$$

$$\frac{\partial H_y}{\partial t} = \frac{-1}{\mu} \sum_{j=1}^{N} \left(E_x\left(r_j^E\right) W_z^H - E_z\left(r_j^E\right) W_x^H \right) V_j \qquad (12)$$

$$\frac{\partial H_z}{\partial t} = \frac{-1}{\mu} \sum_{j=1}^{N} \left(E_y\left(r_j^E\right) W_x^H - E_x\left(r_j^E\right) W_y^H \right) V_j$$

The expanded Maxwell's equations are based on formulations provided by Ala and Francomano with a slight difference in the additional current density term. This term becomes necessary to enable the SPFMax code to simulate interaction between the surface a solid electrode and the charged fluid particles of the fluid model (in this case, the fluid is a plasma). In the propulsion simulation, charged fluid particles take on current from the circuit model, essentially becoming part of it, while simultaneously encompassing the fluid model as well. Certain dynamics of the circuit-fluid model are very different from the circuit-electrode model. Because the electrode is a solid surface, the permittivity, permeability, and conductivity of the circuit material is assumed constant. However, those same properties must be interpolated in the plasma because the plasma is deforming and accelerating over the course of the simulation. As particle concentration changes, physical properties change.

The magnetic nozzle, such as shown below in Figure 12, is needed for our propulsion concept because the high temperatures reached by the plasma will cause rapid erosion and failure of material nozzles, and even if those limitations can be overcome by controlled ablation off the wall, significant weight penalties will be incurred by the additional radiative cooling needed. Towards the goal of studying pulsed magnetic nozzles, we developed a series of verification tests to provide confidence in the numerical output of the gasdynamic physics of SPFMax, and proceeded to study the effects of pulsed gas nozzles (see Figure 13). The purpose was to take a first step in understanding some of the basic physics of expansion from initial hot, cylindrical targets into directed thrust.
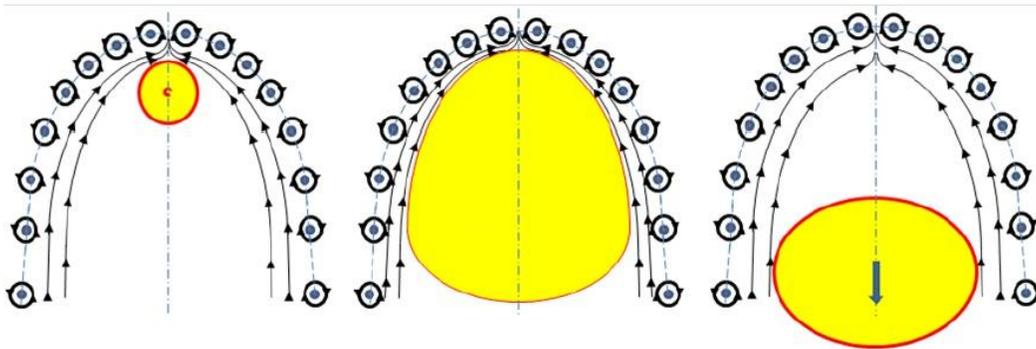

**Figure 12 – Pulsed magnetic nozzle operation (Ref. 10).**
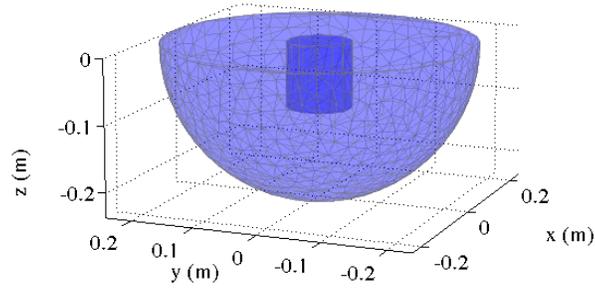
Figure 13 – SPFMax model of a solid state gas nozzle.

A shock tube model was studied that allows for testing and debugging of key physics for flows commonly found in nozzles, including a mixture of subsonic and supersonic flows, shock waves, and thermal expansion. We demonstrated convergence as we increased particle resolution, and the average error for 10,000 particles (particle scale length of ~.1 to 1 cm) was within 5%. We note that higher accuracy can be achieved by increasing the number of particles, but settled on this problem size since 3D simulations could be accomplished in a few minutes for most cases.
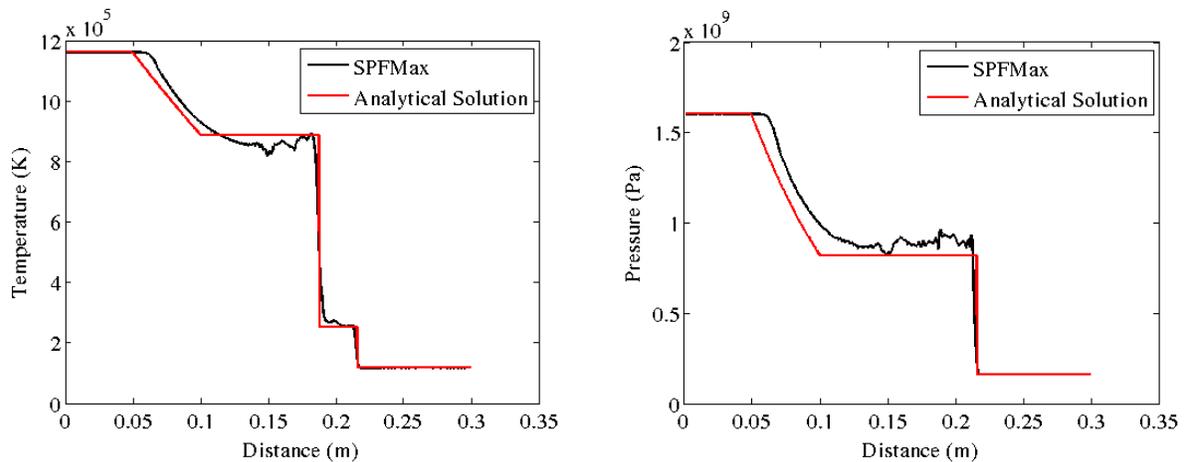
Figure 14 – Temperature and pressure in a shock tube with temperatures between 10 and 100 eV.

We then ran a spherical gas expansion test. For this model, we expect that the particles should expand isotropically with a mean expansion velocity approaching $_{max} = \sqrt{2C_v T_0}$. A sequence of three particle scatter plots shows that there are not anomalous motions and the particle expansion behaves as it should. Figure 16 shows that the mean expansion velocity does indeed approach the predicted result,

which is an indication that isentropic expansion is modeled accurately and that energy is conserved in the time integration algorithm.
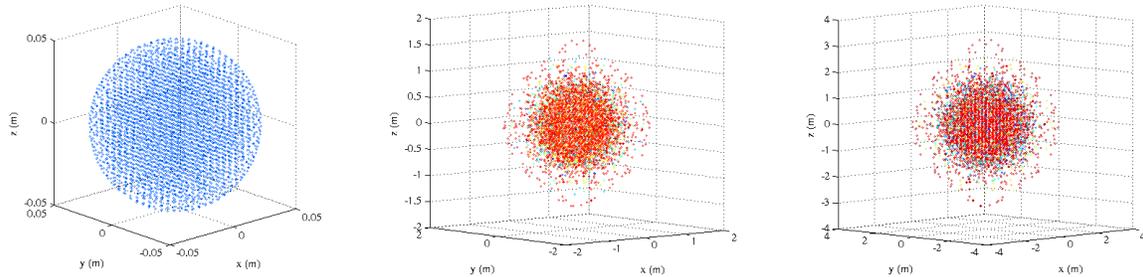
Figure 15 – Spherical gas expansion at 0, 10, and 20 μs.
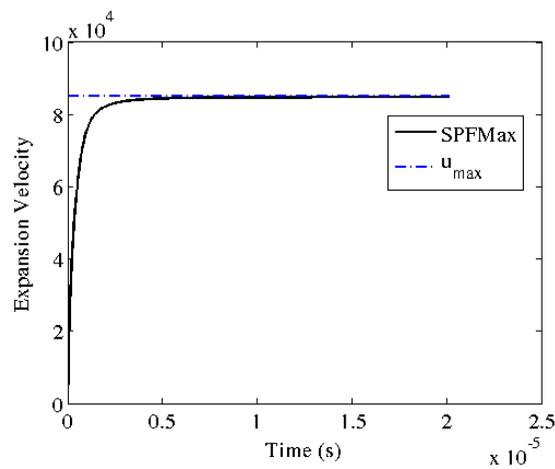
Figure 16 – Mean expansion velocity for spherical expansion test.

For the pulsed gas nozzle tests, we explored over a hundred different cases involving effects of initial nozzle radius and relative position, size, and length to radius ratio of a cylindrical gas target, as well as effects of initial density and temperature. The geometric parameters are illustrated in Figure 17. We found that 'pancake' like initial targets with radii matching the inner nozzle radius at the exit, placed near the nozzle exit, gave the highest propulsion efficiencies (directed kinetic energy divided by initial thermal energy). Figure 18 shows the initial conditions for such a nozzle along with late time expansion once most of the mass has exited. There is some divergence in the plume, which contributes to the 30% or so energy not converted to directed kinetic energy. In this example, the efficiency approaches 70% with an Isp of 6500 s.
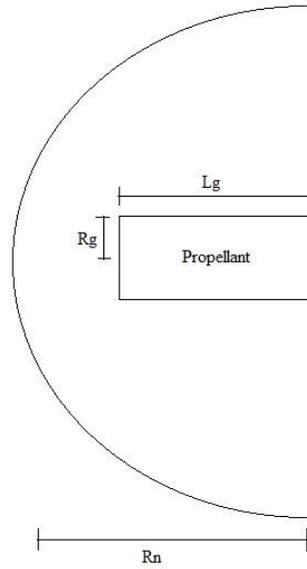
**Figure 17 – Cross-section of nozzle and propellant.**
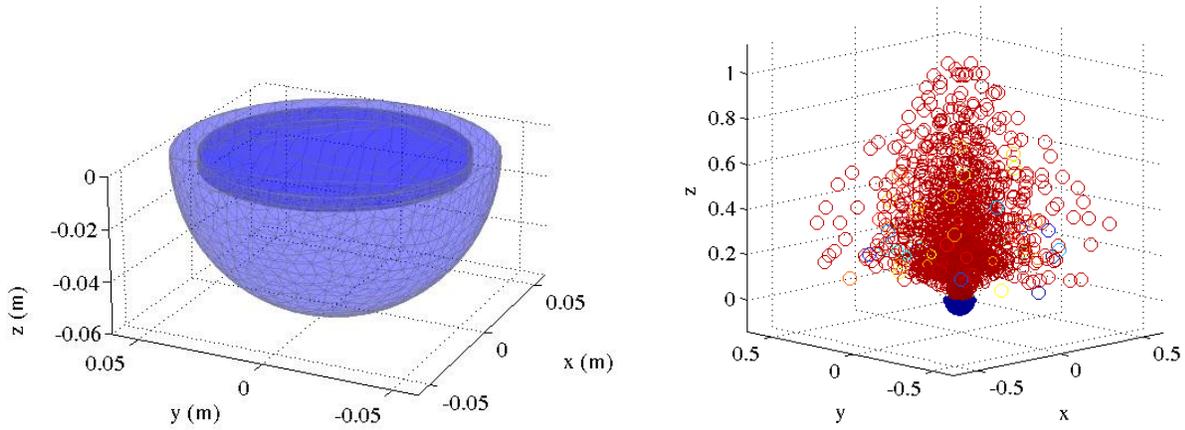
Figure 18 – Initial conditions and late time expansion phase for one of the high efficiency nozzle configurations.
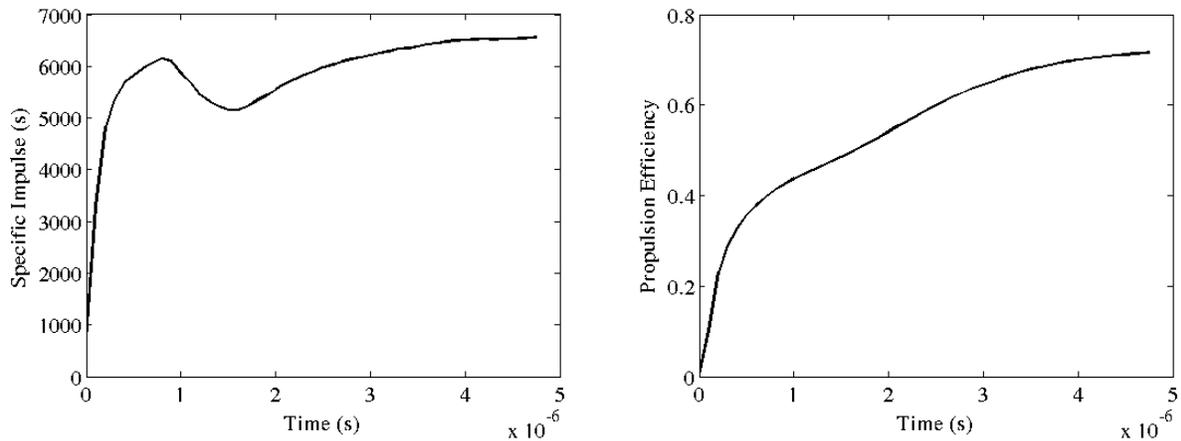
Figure 19 – Specific impulse and propulsion efficiency vs. time for the case in Error! Reference source not found.**. Note the specific impulse dips around 1 as while the gas 'bounces' off the wall. The run is stopped once 95% of the mass has exited the nozzle.**

We anticipate that the physics of expansion in more realistic cases with a magnetic nozzle are going to be somewhat different. For example, the plasma will compress the magnetic field, and perturbations at the vacuum field/plasma interface may cause instabilities. The targets will likely have strong gradients which will modify the expansion behavior. Finally, finite resistivity and other diffusive processes will trap plasma on the field. As we develop the code further we will explore these effects hopefully in parallel with an experimental program. We view the gas nozzle results as a point of reference for idealized behavior, and in doing so this may inform designers on how to properly design targets integrated into magnetic nozzles.

Engine Performance and Vehicle Architectures

A proper assessment of propulsion system performance can only be obtained by incorporating the system into a vehicle design and then flying it on a number of realistic missions. To assist in this effort a simple mass estimation tool has been developed to enable the PuFF team to 'build' a range of vehicles as needed to support the performance evaluation effort.

This model is based on a vehicle study that was conducted in support of a previous Z-Pinch propulsion concept study (Ref. 11). The vehicle, which is shown below, was designed to conduct several missions in the inner solar system, including a crewed Mars mission, with 90-day (each-way) interplanetary transit times. It forms a good basis for evaluating PuFF performance because most of its major components are of the same type as those that will be required on a PuFF vehicle (e.g. tanks for both D-T and lithium). The only minor exception is the uranium storage and supply system that will be required for PuFF.
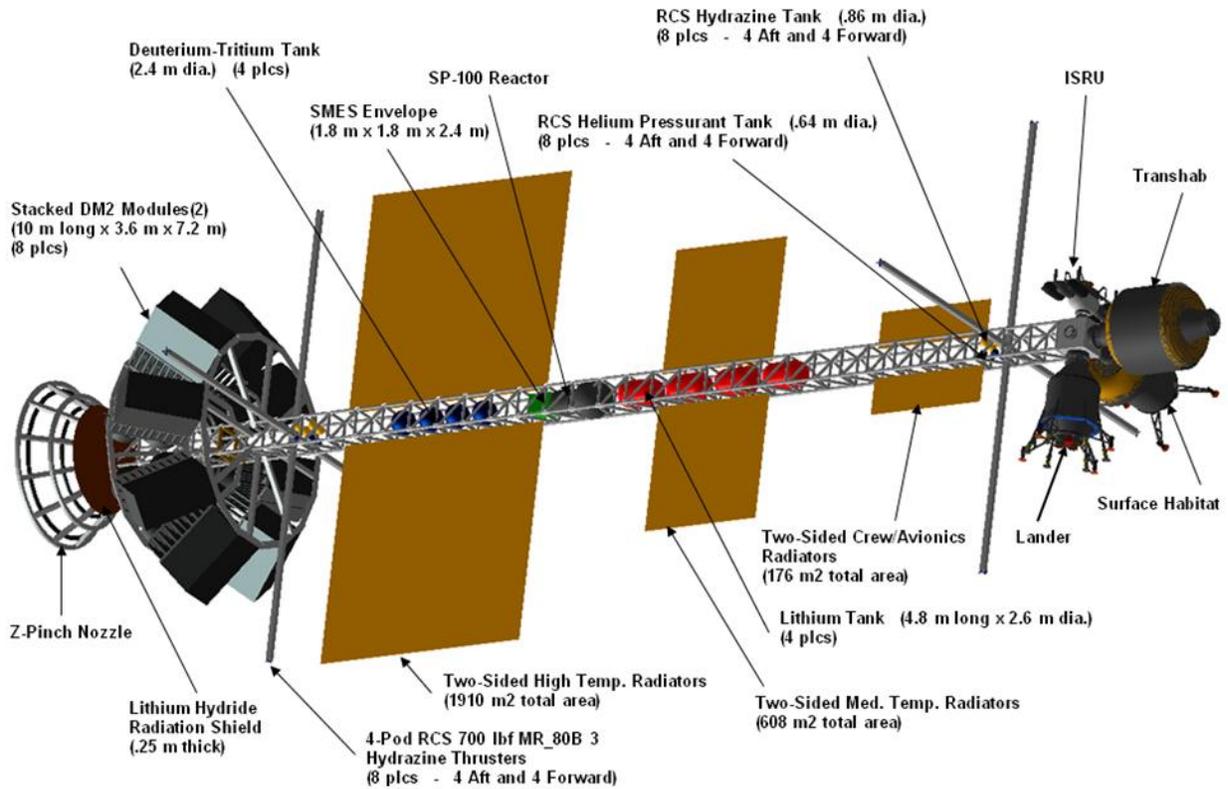
Figure 20 – Vehicle Configuration for Mass Estimation Tool

The major vehicle components and their approximate scaling rules are as follows.

Vehicle Component:	Mass Scaling Rule:
Magnetic Nozzle	Linear with energy generated per pulse
Radiation Shielding	Linear with energy generated per pulse
D-T Tanks	Linear with total mass of D-T mixture carried
Lithium Tanks	Linear with mass of lithium carried
Main Vehicle Truss	Linear with vehicle wet mass and vehicle length
Other Primary Structures	Linear with vehicle wet mass and vehicle length
Secondary Structures	20% of 'Other Primary Structures' mass
Capacitor Banks	Linear with energy input required per pulse
Marx Generator Circuitry	6% of 'Capacitor Banks' mass
Reaction Control System	Linear with vehicle total wet mass
Low Temperature Heat Rejection System	Linear with low temperature heat rejection rate
Medium Temperature Heat Rejection System	Linear with medium temperature heat rejection rate
High Temperature Heat Rejection System	Linear with high temperature heat rejection rate
LN2 Seed Coil Cooling System	Linear with energy generated per pulse
Vehicle Power System • Based on SP-100 reactor and associated power distribution equipment	Linear with maximum electrical power requirement for the vehicle
Avionics System	Constant

It must be emphasized that the model is only intended to provide an approximate vehicle mass. It will be noted that there is no mass margin allowance illustrated above. A 30% 'mass growth allowance' was used in the original source study, use of the approximate scaling rules above will yield an approximate inert mass margin based on the 30%

An example of the model output is given below in Figure 21, where the vehicle dry mass is shown as a function of the medium temperature heat rejection rate. Curves are given for a range of high temperature heat rejection rates (from 100 to 600 MW). And clearly demonstrate the importance of rejecting as much of the total heat load as possible at high temperature.
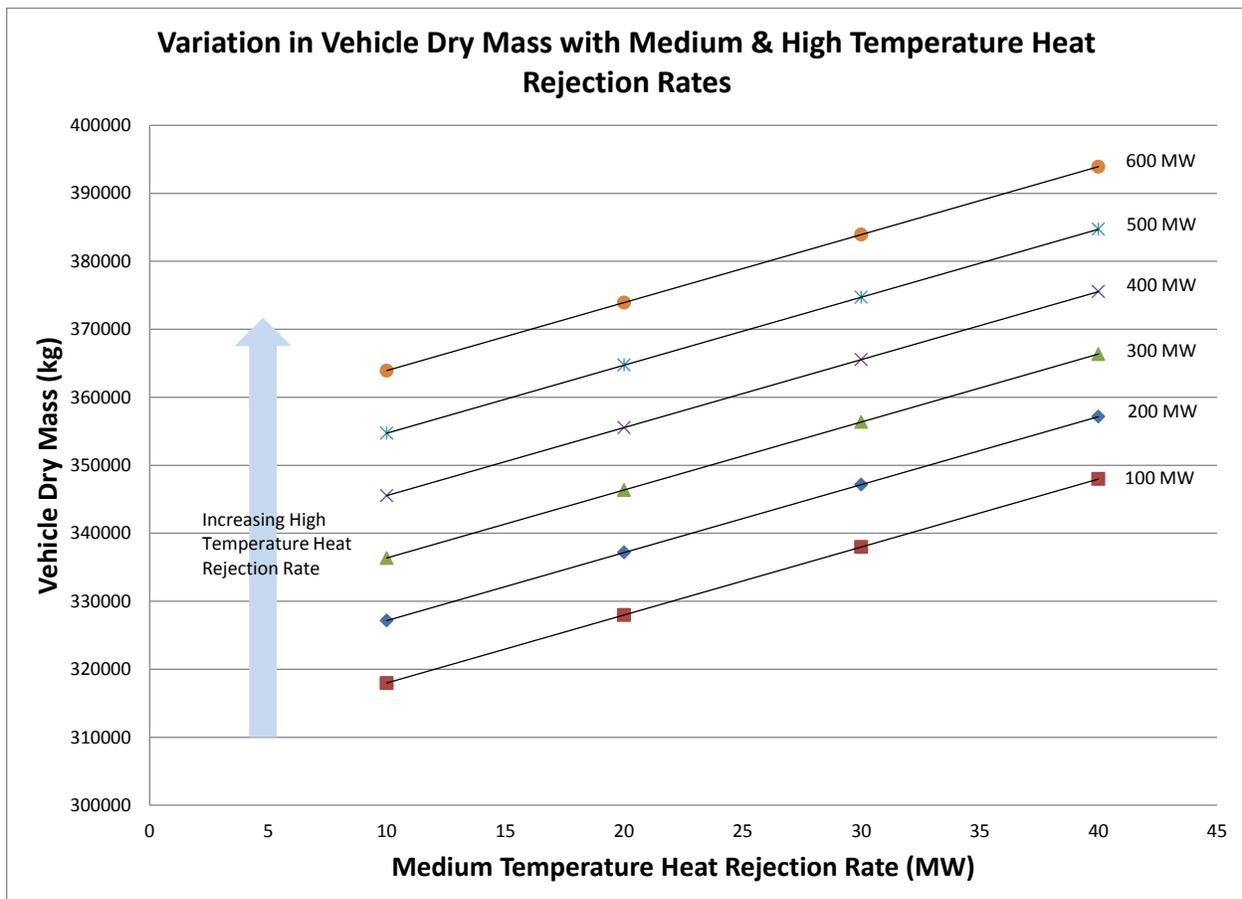
Figure 21 – Sample Output from Vehicle Mass Estimation Tool

Using the point design defined from Figure 11 we resized the vehicle shown in Figure 20 for a couple of new missions. The first mission was a sprint to Mars, carrying crew or payload to support a Martian outpost. The engine was set by the point design, and the missions shown in Figure 22 represent our best effort to optimize performance around the point design. For instance we determined that the point design engine can carry a 25 mT capsule from Earth to Mars in 37 days. The Initial Mass in Low Earth

Orbit for this concept is 190 mT, as shown in the table below. This mass could be lofted to orbit using a Block I and a Block II Space Launch System (SLS).
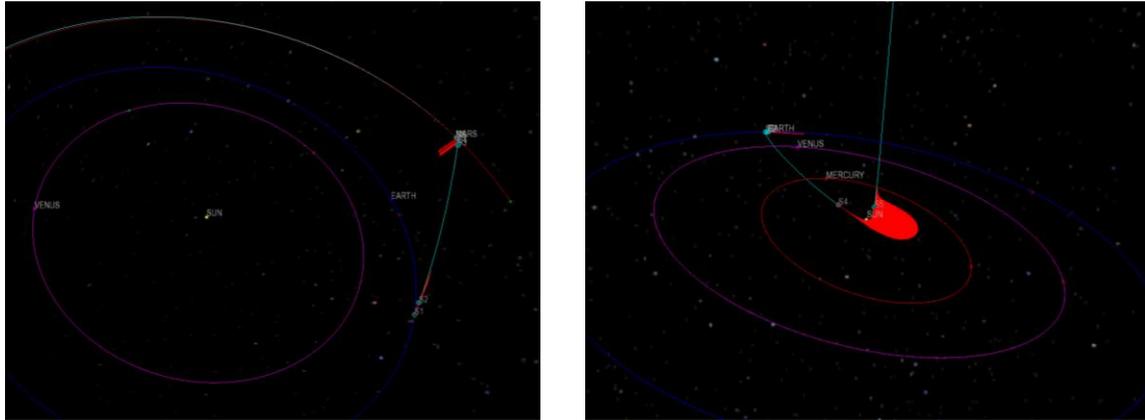

Figure 22 - 37 day sprint mission to Mars and a robotic TAU (thousand AU) mission

We also looked at the same point design for a robotic explorer to the outer solar system. Here we designed a vehicle that starts out at LEO at 150 mT and is capable of delivering 10 mT of payload to interstellar space. The terminal velocity of the vehicle is 0.075 AU/day translating to passing the termination shock in 5 years, a distance of 275 AU in 10 years, reaching the solar gravitational lens in 20 years and achieving 1000 AU (0.016 ly) in 36 years. Such a mission could be completed in the lifetime of a single researcher, providing a wealth of information about local interstellar space and our own solar system's interaction with it.

Table 1- Mass Breakdown for Mars Direct and TAU mission concepts

Subsystem	Mars Express	TAU Mission
Magnetic Nozzle	14.83 mT	14.83 mT
Radiation Shielding	14.01	14.01
D-T Tankage	5.0	5.0
Li Tankage	1.45	0.94
Truss	2.71	2.09
Other Primary Structures	0.64	0.49
Secondary Structures	0.13	0.10
Capacitor Banks	2.10	2.10
Marx Generator Circuitry	0.13	0.13
RCS Wet Mass	1.03	0.79
Low Temp Heat Rejection	1.30	1.30
Medium Temp Heat Rejection	14.82	14.82
High Temp Heat Rejection	1.26	1.26
LN2 Seed Coil Cooling	8.41	8.41
Auxiliary Power	4.40	4.40
Avionics	0.39	0.39
Payload	25.00	10.00
Dry Mass (without MGL)	**94.87**	**77.57**

Mass Growth Allowance (30%)	40.66	35.21
Total Dry Mass	**135.53**	**112.78**
Fuel	56.02	37.03
Total Wet Mass	*191.55*	*149.81*

One challenge in mission analysis is to quickly and accurately evaluate a number of solutions for a given trajectory. Figure 23 below illustrates what is colloquially known as a 'porkchop' plot, a plot of required escape velocity for departure and arrival dates. This plot is for the Mars 2033 opportunity. A normal plot created by hand, attempting to optimize Copernicus, or a similar trajectory system, would demonstrate a number of rough edges, islands and points where data was not acquired. A new program, called CopperKnit, repeatedly interrogates Copernicus with different starting vectors to assist and force Copernicus to find more stable solutions. As can be seen in the figure, CopperKnit greatly assists Copernicus' built in numerical solvers to find needed solutions. CopperKnit is also a batch solver and can generate a plot like the one below in a couple days generally. CopperKnit was developed in parallel to the NIAC effort and in anticipation of a Phase II effort to do a more complete mission analysis. CopperKnit will be integrated into the Phase II effort.

C3 contour plot for the Mars 2033 window. C3 minimum = 11.13 MJ/kg. LEO inclinations from 28 to 29° (±0.005°).
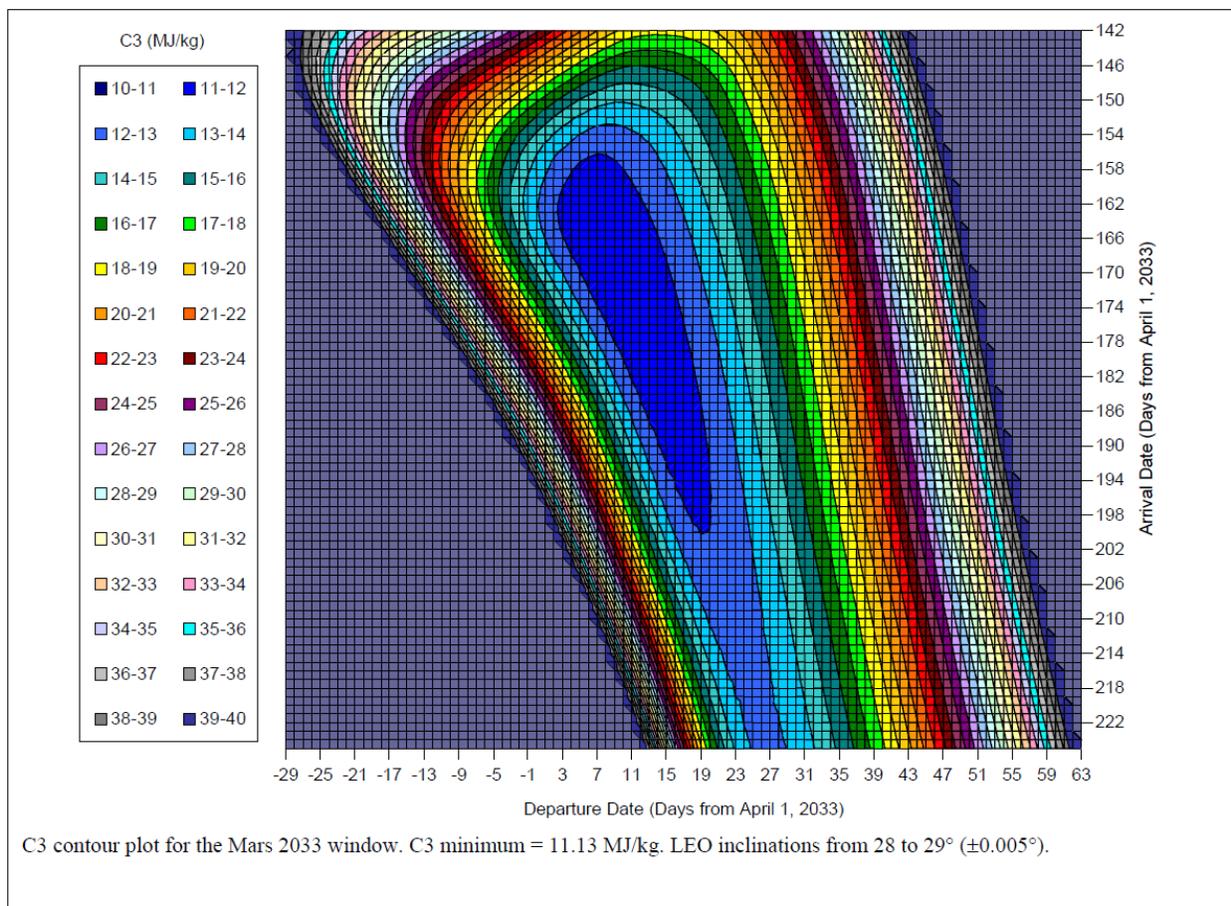
Figure 23 – Sample Output from CopperKnit Tool

Experimental Efforts

As we continued along the path of developing the solid shell uranium target with a D-T core we realized that we would not be able to enhance SPFMax with the needed additional equations for stresses in solids as well as phase change relations in the time permitted. We continued those efforts at roughly the pace anticipated in the Phase I proposal but vectored additional resources into preparing for a future experimental effort. To this end we pulled out several pulsers of various power levels and set them up for future research. Additionally we found diagnostic equipment and refurbished them. Finally we did a few test shots to prove our experimental approach. The results of these efforts are described herein.

PA-80 development

The PA-80 requires an external power supply to charge the 0.75 mfd 80kV capacitor used to store its pulse energy. The requirements for safety and electrical isolation and the desire for reasonable cost led us to design this supply as a pulsed power supply which we call the Pulsed Power Charger (PPC). This section describes the work performed to design, build and test the PPC.

The basic requirements to which the PPC was designed are as follows:

- The PPC must be capable of charging a 0.75 mfd capacitor in series with a 7500 Ω resistor to 80,000V in less than 10 minutes
- The PPC must be fully isolated from all ARC power systems when charging the PA-80. There must not be any conduction path from the PPC to any other ARC circuit while the PPC high-voltage pulse charging circuit is active.
- The PPC must be realized as a separate, self-contained circuit connected to the PA-80 only by an RG-218 high-voltage cable. The PPC must be easily disconnected from the PA-80 and capable of charging other similar energy storage devices as well.
- The PPC must be sufficiently insulated from its surroundings so that there is no electrical leakage to any other objects.
- The PPC must be operable within the safety guidelines set forth by the manager of the ARC.
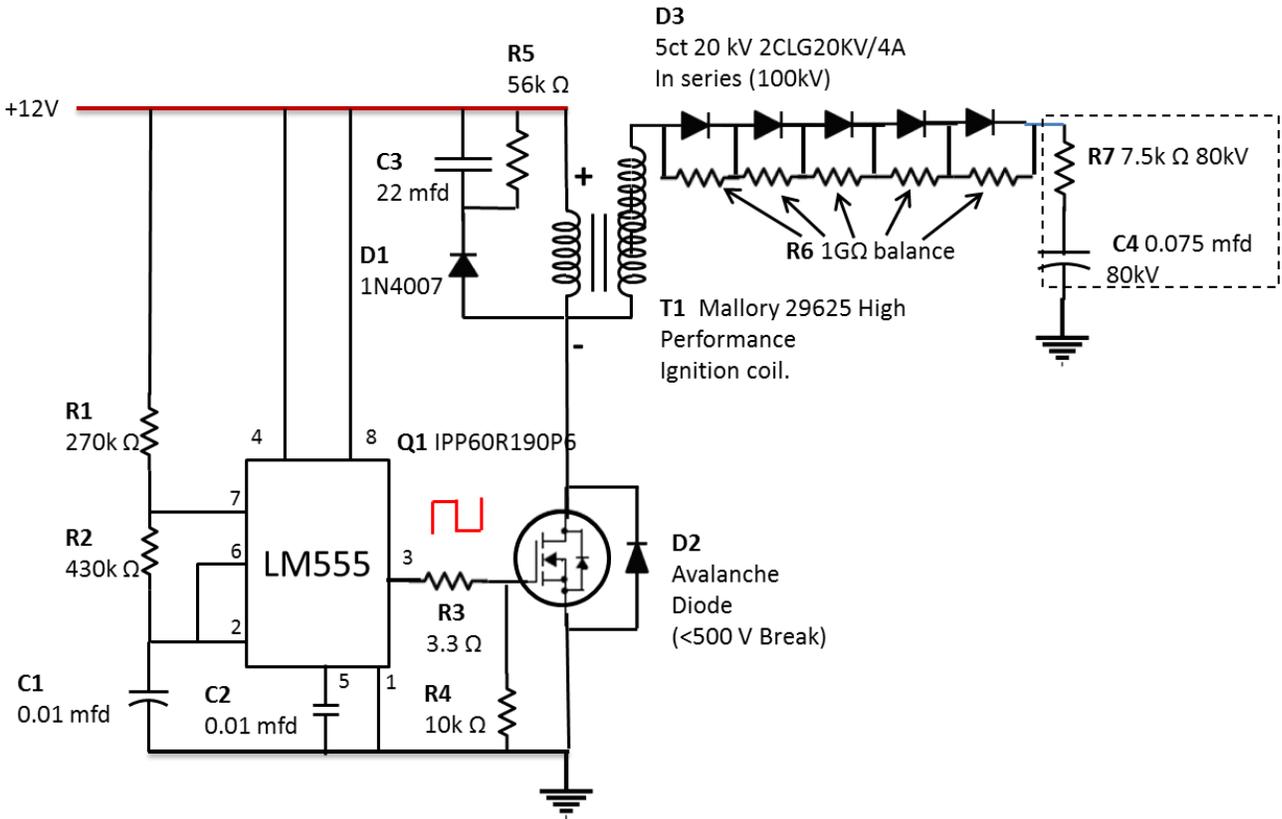
Figure 24 – Schematic for the PPC.

The circuit discussion below is in reference to Figure 24 above and its nomenclature.

Since the circuit required complete isolation from all other power systems, we chose to power the PPC with an independent 12V sealed lead-acid battery. In operation, the battery is fully charged with a separate, off-the-shelf battery charger and then connected to the PPC where it supplies energy for potentially multiple charges to the PA-80 until it requires recharging. The battery chosen was a Chrome Battery 12V 18Ah SLA with T3 connectors.

The LM555 timer is configured to generate a square wave at pin 3 at a frequency determined by R1, R2 and C1. During each cycle, pin 3 will be high (12V) for 5ms and then low (0V) for 3ms. Thus there will be 125 cycles / second in this configuration. This timing will likely be adjusted in the future to optimize the charge rate.

Each rising edge of the square wave turns on Q1 causing current to flow through the primary winding of T1. As current flows, a magnetic field builds in T1, peaking toward the end of the 5ms on-time. The falling edge causes Q1 to abruptly switch the current off, causing the magnetic field to collapse through the secondary windings of the transformer. This generates a > 80kV pulse across the secondary winding on each cycle.

Each 80 kV pulse briefly charges C4 (the PA-80 capacitor). Because the capacitor cannot discharge back through D3, charge accumulates in C4. As C4 charges, the voltage across it rises from 0 to 80kV. The PA-80 charge monitor senses the voltage and turns the PPC off when the voltage across C4 reaches 80kV (or a lower desired voltage).

Because the leakage inductance of T1 causes significant voltage spikes across Q1 during operation, the snubber circuit consisting of D1, C3 and R5 was added to suppress them.

The switching transistor Q1 is a P6 Super Junction 600V MOSFET from Infineon. It was chosen for its high current rating (20A) and its extremely fast (10's of ns) switching times. T1 is a high-performance automotive ignition coil. Several different coils were traded to determine the best performer for this application. The best by far was the Mallory 29625 Pro Master coil. This ignition coil was developed for street-rod use and boasts a 67 kV rating when used with a high-performance automotive ignition system and spark plugs. When driven with the much faster P6 MOSFET through a 2cm spark gap, it easily delivered over 150kV for more than 5 microseconds per cycle without any internal arcing. Its measured inductance was only 1.5 mh, suggesting that it could easily be pulsed at > 1khz with no appreciable loss of performance.

The circuit up to and including the coil, but excluding the large high-voltage series diode bridge (D3 & R6), was assembled on a single polypropylene sheet (see Figure 25 below).
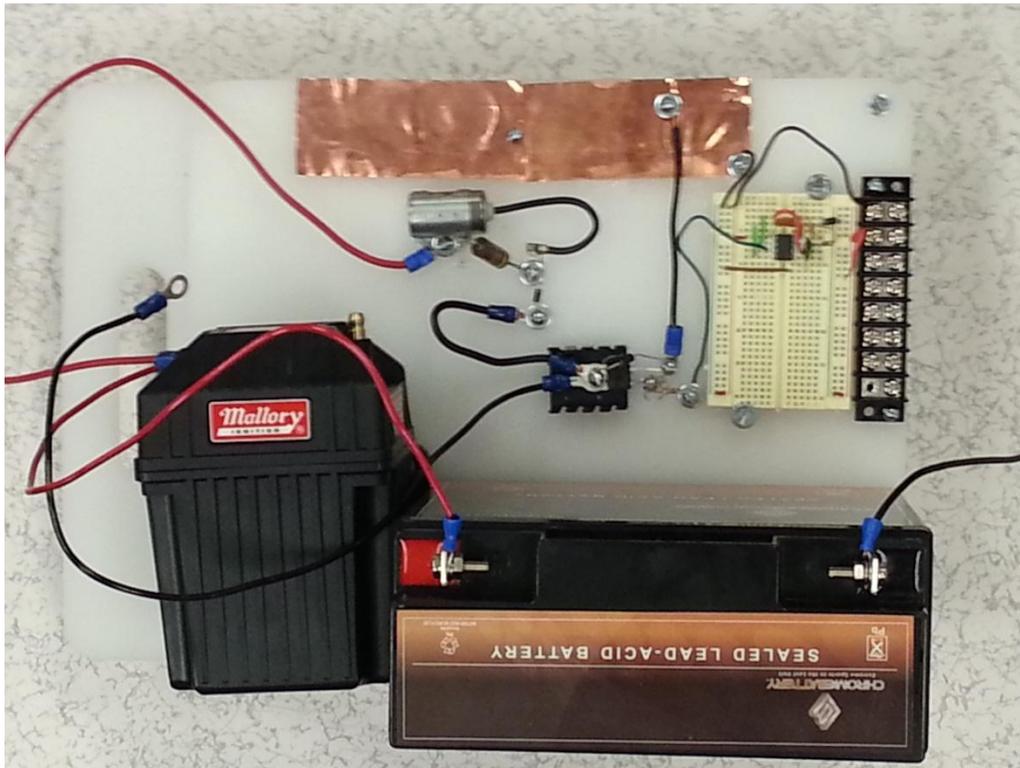

**Figure 25 – Pulse Generation Circuit for the PPC.**

The high-voltage diode bridge is currently submerged in transformer oil for testing, but is expected to be housed in an insulating tube after testing is complete. It is shown with the 100kV test capacitor (white plastic) below in Figure 26.

Figure 26 – 100kV diode bridge and test capacitor.

The initial testing of the PPC consists of the following:

1) **Spark-Gap test** – The PPC was discharged across a 2cm spark gap. The voltage across the gap was measured with an oscilloscope connected through a 10k : 1 voltage divider as shown below in Figure 27:
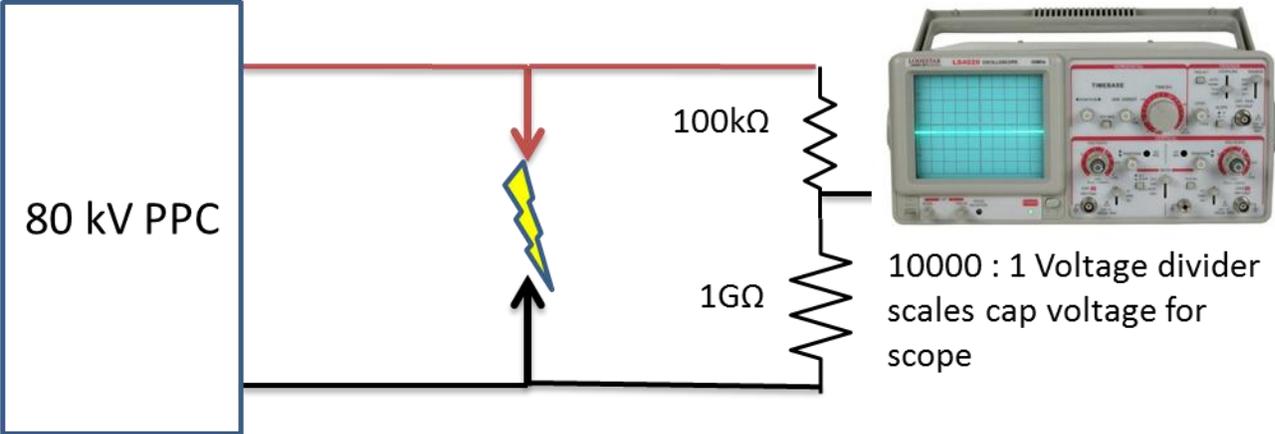
Figure 27 – Spark Gap Test Circuit.

The test showed the PPC delivering >150 kV peak voltage per cycle. Shorter gaps reduced the peak voltage somewhat and lengthened the pulse time.

2) **Capacitor charge test –** The PPC is used to charge a Maxwell 31235 100kV test capacitor to 80 kV. The capacitor is then allowed to discharge through the measurement voltage divider slowly. The voltage is monitored during both charge and discharge. The test setup is shown below in Figure 28:

5 20kV Diodes in series to make 100kV rectifier. 1 GΩ resistor in parallel with each diode to assure even voltage drop.

80 kV Charge Circuit

'Safety Valve' spark gap set to break down at 85kV

100 kV 0.317µf Capacitor to be charge to 80kV

200kΩ

2GΩ

10000 : 1 Voltage divider scales cap voltage for scope & allows cap to discharge safely over 2 hrs
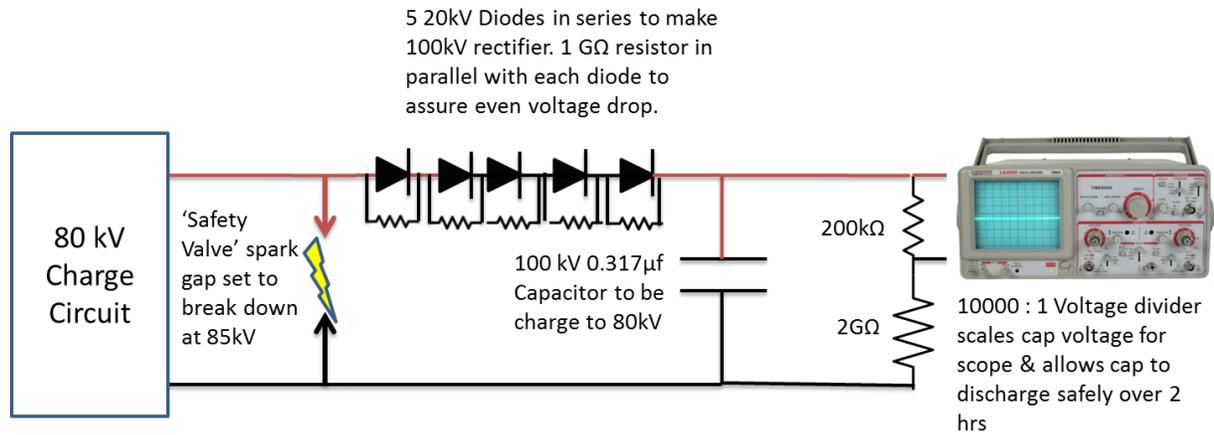
Figure 28 – Charge Test Circuit.

1 kJ Pulser

In addition to its role as a test capacitor for the Pulsed Power Charger, the Maxwell 31235 100kV capacitor may be used to store energy for high voltage, medium energy Z-Pinch experiments.

Figure 29 – 1kJ Pulser ready for test.

Charged to 80kV, this capacitor stores 1014 J which may be dissipated into an experimental load when the capacitor is switched with a spark gap trigger. The diagram below (Figure 30) illustrates:
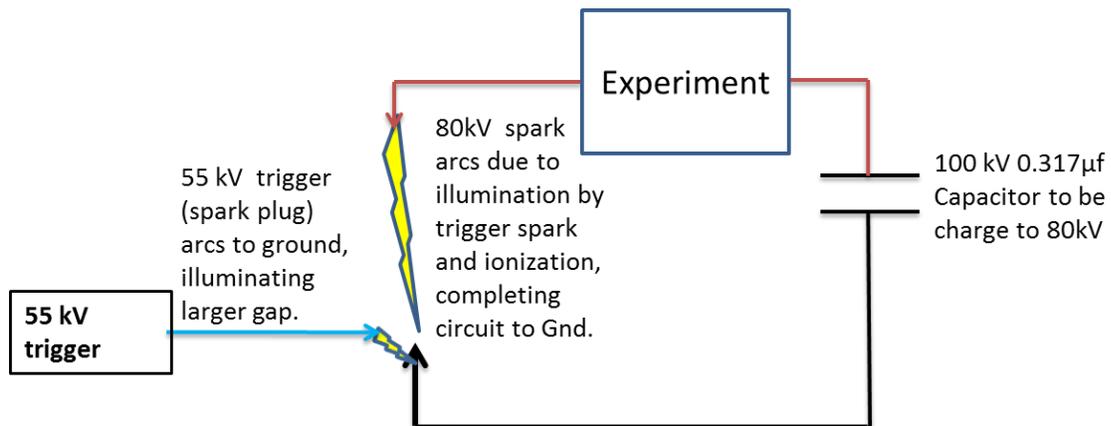
Figure 30 – Trigger Operation.

The trigger uses a conventional automotive spark plug. The plug is screwed into the ground plate, adjusting the length of the gap. The other plate is connected to the experimental load. The trigger is shown in the photo below (Figure 31):
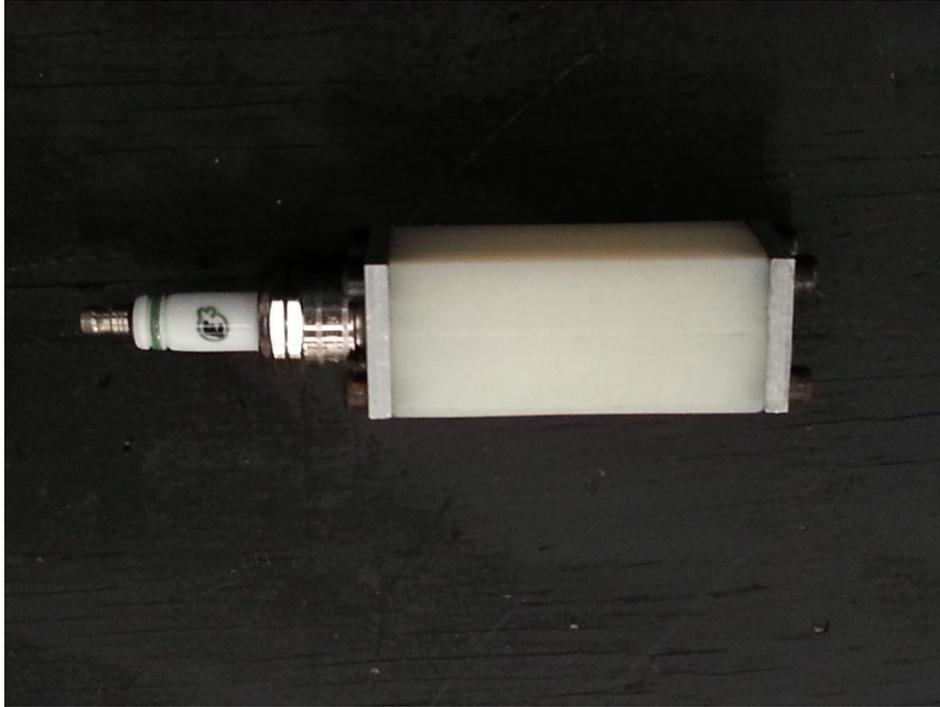
Figure 31 - 55kV Trigger Assembly

MMG Facility Refurbishment

The MSFC Micro-Meteoroid Gun (MMG) is triggered by an exploding wire. The plasma from the exploding wire accelerates projectiles up to 7 km/sec under a very short range. This system has been operational since 2008. This system includes Sorrento Electronics 40 kV units that are to be charged to less than 22 kV in its current configuration (due to atmospheric breakdown at higher voltages). It is capable of discharging at 7.5 amps at maximum voltage and can be extended to double that current with additional capacitors.

In order to demonstrate a Z-pinch plasma, a means for near instantaneous vaporization of a lithium wire by capacitor discharge is required. The MSFC Exploding Wire Gun (EWG) facility employs a triggered discharge of up to 4 capacitors each capable of storing 4kJ at 22kV. A small vacuum chamber was fitted with a custom-built, non-conductive flange designed to integrate with the EWG with a minimum of system modifications (see Figure 32).
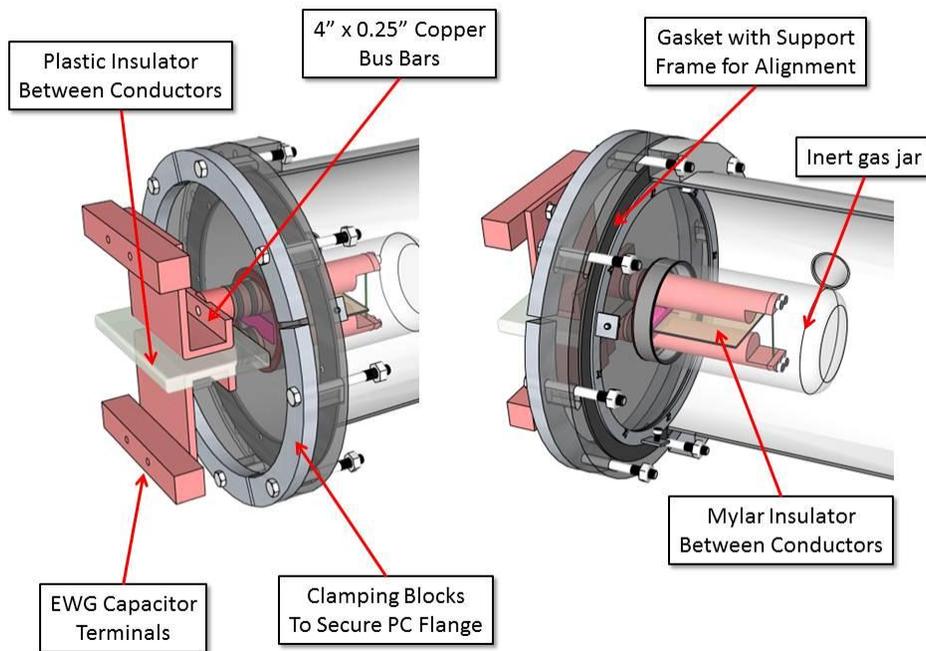
Figure 32 - General configuration of plasma containment chamber with lithium wire support conductors.

The flange is polycarbonate to facilitate custom machining for double O-ring seals along each conductor and a single face-sealed O-ring interfacing with the chamber flange.

Figure 33 - Machined copper conductors showing double seal O-ring grooves.
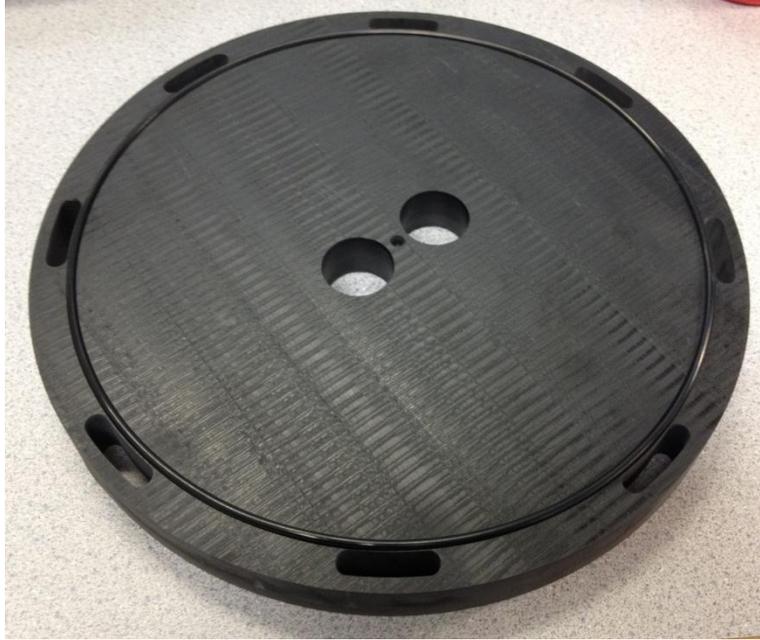
**Figure 34 - Polycarbonate flange showing O-ring face seal and conductor glands.**
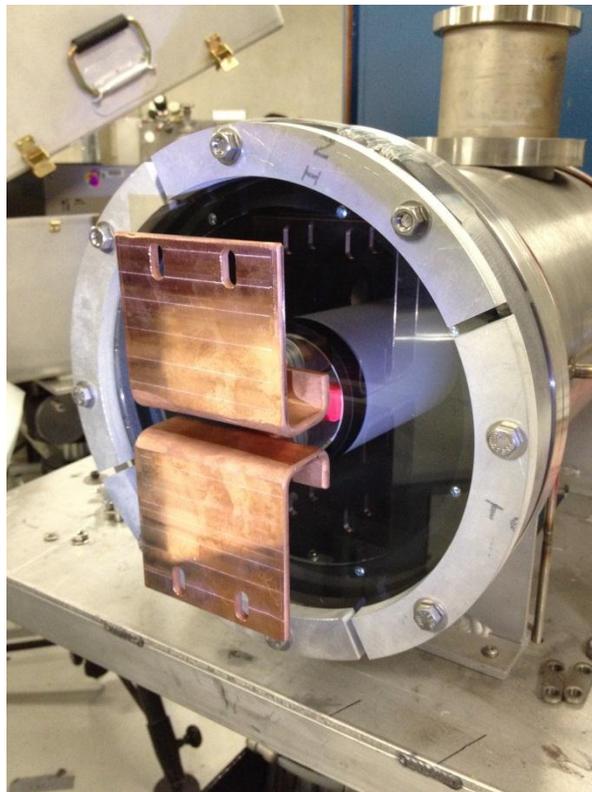
Figure 35 - As built plasma containment chamber showing EWG mating conductors.

The plastic jar provides a protective gas cover for the lithium wire which is installed between the conductors inside an alkali metal handling glove box. The entire flange with wire is then transported to

the EWG facility (in the same building) to be installed in the vacuum chamber. In this way, the wire is protected from oxidation and handling damage until ready to test.

Experimental Diagnostics
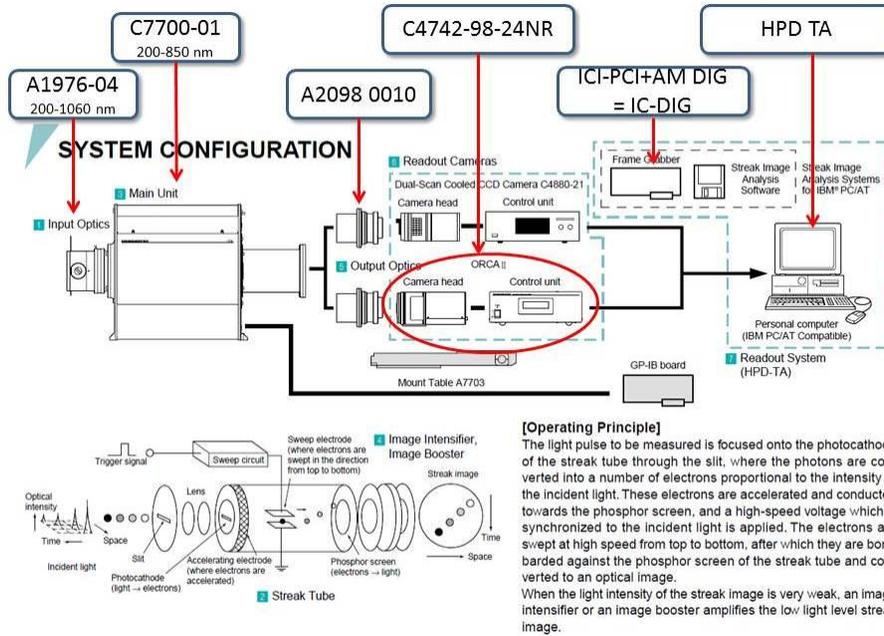
Figure 36 - Streak Camera Configuration Overview

The Hamamatsu streak camera is designed to visually capture electromagnetic phenomena of very short duration, providing an intensity field plotted vs. both time and distance. The streak camera is capable of capturing events with a resolution as short as 5 picoseconds (5E-12 seconds) while capturing data for a duration as short as 5 nanoseconds (5E-9 seconds).

All of the associated components of the system were gathered together and integrated into an existing RF shielded case designed to preclude interference from spark-gap triggering of a high energy capacitor bank (4 kJ).

A literature review covering streak cameras was conducted to gain substantial operational knowledge prior to system setup. All components of the system were subjected to a thorough visual inspection and then integrated together for trial operations. The motherboard battery for maintaining the real time clock had to be replaced in order to boot up the Windows 98/NT-based PC. The commissioning procedures outlined in the operator's manual were followed to gain familiarity with the user interface, known as HPD-TA (High Performance Digital Temporal Analyzer). The HPD-TA provides a relatively user-friendly environment to adjust performance settings and to control image capture.

Of primary concern was a reported inability to trigger the streak camera, thus rendering the system unusable. Hardware trigger signal adjustments were made and triggering was successfully demonstrated by capture of an image of a microcontroller pulsed single LED with a very uniform period (44 microseconds).
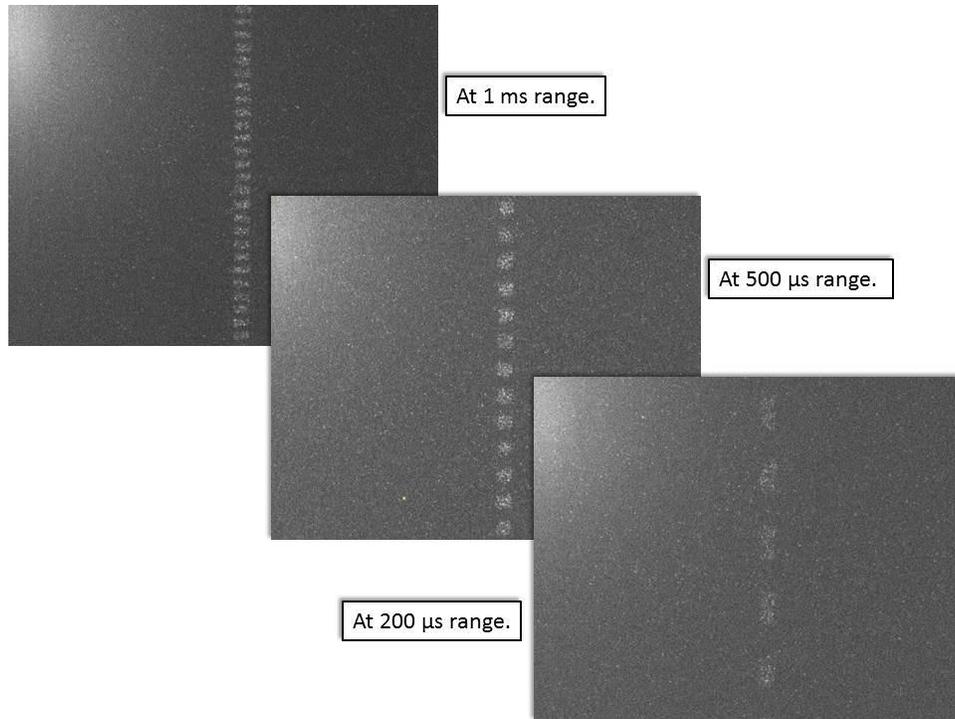
Figure 37 - First Captured Images of flashing LED, approximately 22.7kHz (44 microsecond period), horizontal axis is position in space, vertical axis is position in time.

A variety of image adjustments and triggering configurations were made using the single LED setup. The single LED pulse frequency was too slow to test streak duration ranges shorter than 200 microseconds.


Figure 38 - Four LED timed light sequencer, horizontal spacing is 15.2 mm.

A string of four, equally spaced LEDs was fabricated and setup to receive individual triggers. A Berkeley Nucleonics model 555, multi-channel delay generator is part of the streak camera triggering hardware and was used to program a very precise sequential pattern of LED flashes synchronized with the streak trigger to demonstrate a capture duration of 5 microseconds, consisting of 500 nanosecond pulses timed exactly 1 microseconds apart.
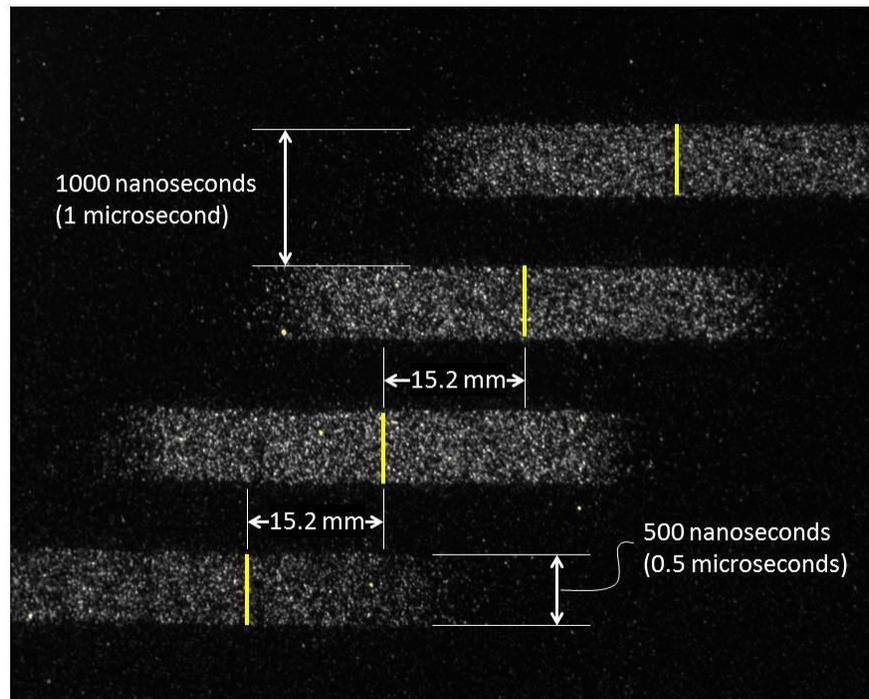

Figure 39 - Four 500 nanoseconds pulses spaced 1 microsecond apart.

The captured images allowed a verification of factory calibration with respect to streak camera internal image capture delays.

Lithium Wire Extrusion

2mm diameter lithium wire was ordered for use in extruding a suitable diameter final wire. In general, a diameter of between 0.4mm and 0.7mm is desired to ensure the wire is the component of the electrical discharge system with the highest resistance. In order to produce a wire of such a small diameter, a threaded-extrusion die was fabricated.
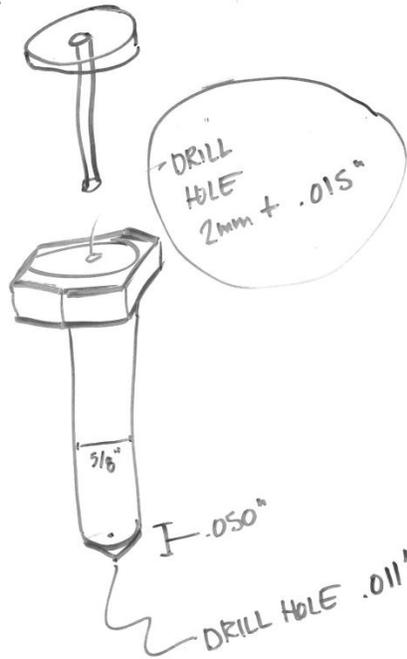

Figure 40 - Lithium extruder concept.

All lithium wire handling must take place under a cover gas or mineral oil. A specialized argon glove box for handling of alkali metals was recommissioned, scrubbed of oxygen and setup for PID loop heater control of the extrusion die body. Prior to delivery of the 2mm wire, small amounts of lithium sample material were melted into the die after which a threaded plunger forced the lithium out through a tiny orifice formed by drilling and peen hardening the end of a carbon steel slug. Lithium has a melting point of 180.5°C.

Figure 41 - Lithium extruder as built. Note heater tape to soften/melt lithium.

A 0.4mm diameter wire was successfully extruded with the die at 170°C. Further adjustments to the extrusion orifice through peening are expected to yield different diameter wires as required. When using the 2mm wire, small (about 25mm) lengths can be slid into the extrusion die without prior melting and tested for room temperature extrusion.
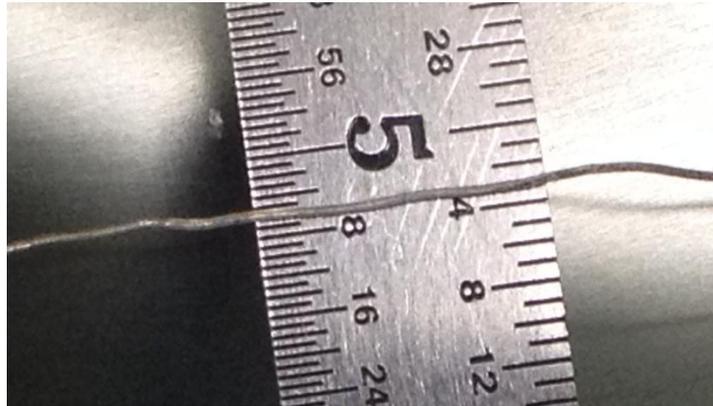

Figure 42 - Extruded wire, approximately 0.4mm (1/64") diameter.

Neutron Detector

A handheld neutron probe/radiation detector is available for use in detecting potential neutron emissions from any lithium wire plasma z-pinch reaction. The polyethylene moderated detector will be placed next to the plasma chamber. If available, a second unit will be located on the opposite side of the vacuum chamber to characterize any asymmetry of emissions.

Figure 43 - Thermo Eberline SWENDI 2 neutron probe with counter.

Alpha, Beta and Gamma (X-Ray) Radiation Detector

A handheld radiation detector is available to place in the immediate vicinity of the plasma chamber to observe and record radiation emissions levels during testing.

Figure 44 - Radalert50 Nuclear Radiation Monitor

Lithium Wire Implosion Demonstration

As a final qualification of the MMG we imploded a 99% pure Li6 wire that we had extruded to approximately 1/64 in (0.4 mm). Figure 45 illustrates the wire setup. Running at 22 kV and 4 kJ we can see in Figure 46 that the MMG was successful in imploding the wire and that the high speed camera was able to capture the progression of implosion. At 12 ns (nanoseconds) the wire just begins to glow and we are barely able to see the ends of the wire connected to the electrodes. At 13 ns the wire glows throughout the length. At 14 ns the image has swollen to several sizes from its original thickness and spalling is apparent. Clearly the wire has vaporized and is expanding through the chamber.
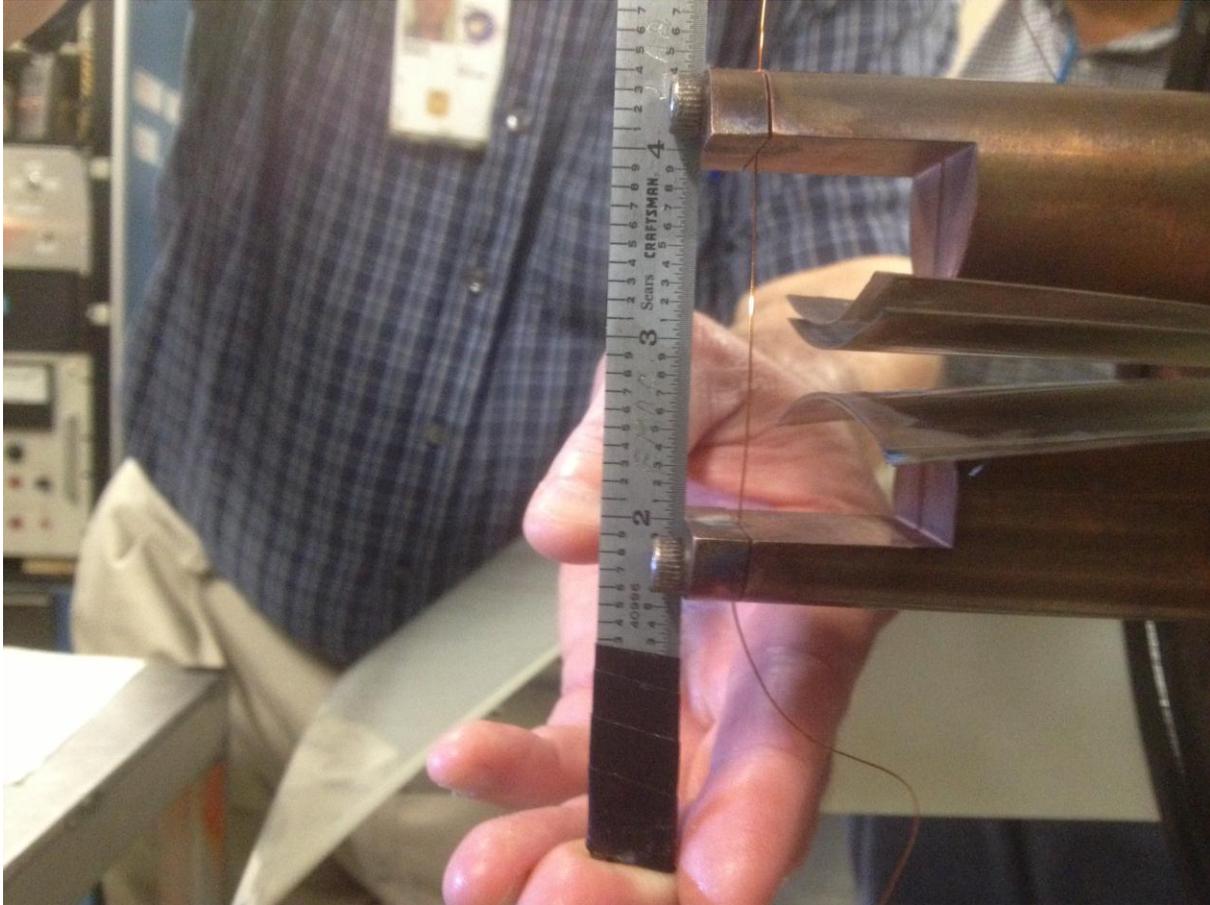
Figure 45- experimental setup of wire in MMG. In this picture copper wire is shown. Our future plans include using lithium wire as well as neutron producing materials.
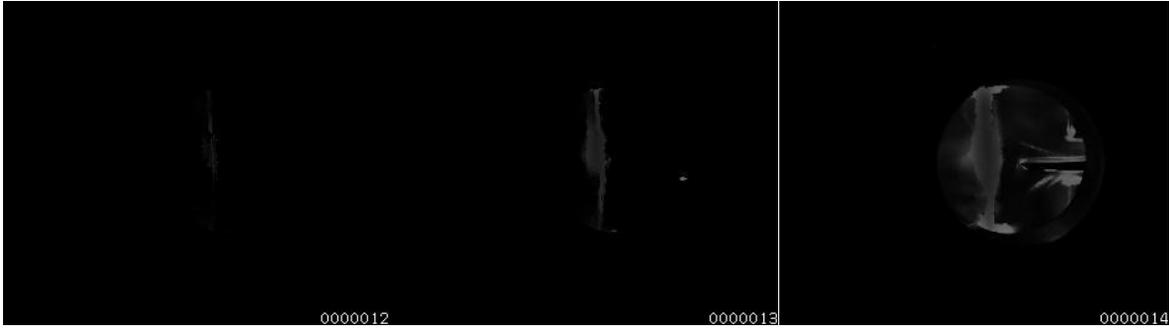
Figure 46 – Test fire of 1/64 in Li wire at 8 kJ, 22 kV, 320 kA. Frame 1 (12 nanoseconds) shows ends of wire starting to glow. Frame 2 (13 ns) shows illumination all along wire and some spalling. Frame 3 (14 ns) demonstrates implosion of the wire and subsequent expansion.

Experimental Plan

The last part of our phase 1 proposal was to identify a promising plan to experimentally explore PuFF potential. As already noted we have set up a 200 J, 1 kJ, 4-8 kJ pulsers with a vacuum chamber and appropriate experimental diagnostics to allow us to test a range of different materials leading up to test articles that would be similar to PuFF targets. Note the progression of power levels on the pulsers; they are roughly on one order of magnitude increments. The future experimental facilities below continue that progression, with the planned assembly of a 67 kJ drag gun and the 572 kJ Charger – 1 facility. This spacing of power levels is highly advantageous to capture plasma creation and propagation. This combination of experimental apparatus will quickly and inexpensively allow the PuFF team to narrow into the optimal target configuration and power requirements.

Future experimental facilities

First our experimental plan anticipates the development of another pulser that was not worked on in the Phase 1 effort. This pulser, a 67kJ Drag Gun. The Plasma Drag Gun energy storage system consists of a capacitor bank made up of four segments with total capacitance of 53.6 µF and storing 67 kJ at a charging potential of 50 kV. Once the desired charging voltage has been reached, a closing switch is triggered, resulting in a current pulse of 1 to 1.25 MA. The current rise time is governed by circuit inductance and is on the order of 300 ns for the facility as currently configured.

This pulsed power system is currently in the initial stages of assembly. The major hardware is in place to be installed, and ready to be connected to the power infrastructure when the main electrical components are set up. The remaining tasks for the assembly are to connect the major hardware components together, install the control system and data acquisition system, and test the system to ensure its nominal operation.

Another facility that is anticipated to be eventually used, but is not planned for our Phase II effort is the Charger 1 facility. The Aerophysics Research Center (ARC), **Figure 46**, is a constituent of the University of Alabama in Huntsville Research Institute (RI), located on Redstone Arsenal near the university campus and enables our NFP Research Center to perform experiments up to the level of Secret. The Fusion Propulsion Research Center (FPRC) Pulsed Power and Diagnostics groups are located at the ARC as well as the Charger-1 pulsed power facility, Figure 46, is housed. The Charger-1 is housed in 5000 ft² of laboratory space, and is supplemented by

Figure 47 - The Charger 1 Pulse Power Research Facility provides 3 TW and 572 kJ of electrical energy into pinch loads.

the ARC's machine shop capable of fabricating parts and components for the experiments. The FPRC Pulsed Power and Diagnostics groups reside in 768 ft^2 of office space, which includes 2 offices and conference room. The controls and data acquisition (DAQ) for the Charger-1 facility, along with controls and DAQ for the PA-80 and 1 kJ machines are housed in the ARC control center: a 800 ft^2 room encased by 2 ft thick concrete walls for ballistic protection and personnel safety.

Experimental plan

To help guide the design of other targets, we have conducted a study looking at energy yield vs pulsed current, and have discovered that under our assumptions, there exists an optimum current for maximizing yield at fixed DT target size as shown the predicted energy yield vs. applied current, Figure 47. This plot was generated as follows. We follow the method of Ryutov et al(2000)[xii] to balance the kinetic energy of the implosion against the thermal energy of the target, where the kinetic energy is derived from the applied current, assumed to be a sinusoidal waveform. We assumed that only 5% of the available capacitor bank energy goes into thermal heating of the target. We assume that the confinement is only 25 ns at the peak temperature. Finally, we assume that the plasma is surrounded by a ^{238}U liner of 3mm uncompressed thickness which has been shock compressed to 1mm thickness. Under these conditions, we find that the total energy yield (fusion charged particles + fission products from fast neutron reactions) is comparable between fission and fission, and that for each fixed mass of DT, there is an optimum current.

The black horizontal lines in this figure represent the energy level of the capacitor banks available to us. The lower one is referred to as the PA-80, and will be the work horse. It is a 200 J system at UAH and will be used to study neutron yield from DD gas puffs. Similarly, we will conduct gas puff experiments in DD on the 1 kJ machine also at UAH. The 3rd line from bottom represents the 4-8 kJ machine at NASA MSFC which will be utilized to study wire ablation with lithium,

lithium deuteride, and hybrid targets using depleted uranium. These will provide the data (neutron yield, xray spectroscopy) to characterize the internal state of the plasma at peak compression, and will allow us to benchmark our 3D codes. Following
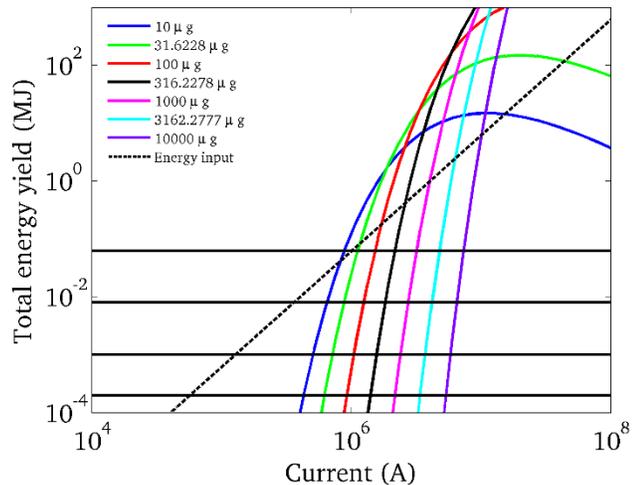
Figure 48 Target energy yield vs peak current assuming 25 ns discharge. Horizontal lines represent the energy level of machines available our program. The various curves are different target masses of DT gas, showing that each one has an applied current which optimizes the yield as a function of current.

testing with the lower energy level machines, we will utilize the 67 kJ machine for high power shots at high energy utilizing lithium or lithium deuteride wires to determine scaling of neutron yield at high energy levels. SPFMax will be utilized to assist in diagnostic analysis (compressed density, peak

temperature), and departures between the model and experiment will help inform departures from local thermodynamic equilibrium in the plasma, a strong indication of instabilities. Scaling laws will be developed to predict the machine size needed for a gain of ~10 to 50, which will inform the design of experiments on Charger 1 (highest horizontal line on Figure 6) and the follow on LTD system to be designed as part of this effort. By conducting simpler experiments at lower energies, it will give us the ability to generate high data rates and supply information for the modeling to assist improved design of breakeven targets driven by appropriately sized machines.

Conclusions

As to be expected for a NIAC Phase I PuFF is a work in progress. However our steady state results illustrate great potential for breakeven energy production and beyond. A non-optimized application of a PuFF engine point design demonstrates game changing capabilities in two missions with expectations of higher reductions from further optimization and inclusion of LTD's. A bulleted list of our accomplishments includes:

Theory

- Verified 3D code on shock capturing and expansion
- Studied pulsed nozzle efficiency
- electromagnetic plasma code nearly complete
- Hybrid Fission/fusion power balance showing much lower energies required for breakeven

Experiments

- Built a complementary team of collaborators prepared to conduct wire array and gas puff z-pinch experiments
- developing and configuring five pulsed power systems with energy levels spanning five orders of magnitude in capacitor bank energy to develop scaling laws for advanced propulsion design

Systems Analysis

- Crewed Mars vehicle delivers 25 mT of capsule, crew to Mars in 37 days starting with a 190 mT vehicle in LEO. Suitable for a Block I and Block II SLS
- Interstellar probe capable of delivering 10 mT to 1000 AU in 36 years, would pass through the termination shock in 5 years. IMLEO is 150 mT, suitable for a Block II SLS and commercial launch vehicle

Acknowledgments

References

1 Dyson, George. Project Orion – The Atomic Spaceship 1957-1965. Penguin. ISBN 0-14-027732-3

2 "An Antiproton Catalyst for Inertial Confinement Fusion Propulsion" by Raymond A. Lewis, Richard Newton, Gerald A. Smith, William S. Toothacker and Randall J. Kanzleiter; AIAA/SAE/ASME/ASEE 26th Joint Propulsion Conference, July 16-18, 1990 / Orlando,. FL

3 "Antiproton catalyzed fusion propulsion for interplanetary missions", B. N. Cassenti and T. Kammash, AIAA, ASME, SAE, and ASEE, Joint Propulsion Conference and Exhibit, 32nd, Lake Buena Vista, FL, July 1-3, 1996.

4 "Hybrid Nuclear Pulse Propulsion", Brice N. Cassenti, AIAA-99-2699.

5 "Nuclear energy: The hybrid returns"; Nature 460, p. 25-28 (2009).

6 "Antiproton Driven Propulsion Systems – Fission or Fusion", by Terry Kammash and Ricky Tang, 41st AIAA/ASME/SAE/ASEE Joint Propulsion Conference & Exhibit, 10 - 13 July 2005, Tucson, Arizona. AIAA 2005-4137.

7 "Muon-Boosted Fusion Propulsion System", by Terry Kammash and Ricky Tang, 43rd AIAA/ASME/SAE/ASEE Joint Propulsion Conference & Exhibit, 8 - 11 July 2007, Cincinnati, OH, AIAA 2007-5609.

8 "Fusion Driven Fission System for Space Surface Power Application", by Terry Kammash and Ricky Tang, 44th AIAA/ASME/SAE/ASEE Joint Propulsion Conference & Exhibit, 21 - 23 July 2008, Hartford, CT, AIAA 2008-4761.

9 http://www.nndc.bnl.gov/exfor/endf00.jsp

10 'Conceptual Design of In-Space Vehicles for Human Exploration of the Outer Planets', Adams, R.B *et al*, NASA/TP—2003–212691.

11 'Z-Pinch/Dense Plasma Focus Thermonuclear Propulsion System', by the Advanced Concepts Office (ED04), Marshall Space Flight Center, October 8, 2010.

[xii] Ryutov, D. D., M. S. Derzon, and M. K. Matzen. 2000. "The Physics of Fast Z Pinches." Reviews of Modern Physics 72 (1): 167.